

MOBIUS: A Multi-Modal Bipedal Robot that can Walk, Crawl, Climb, and Roll

Alexander Schperberg¹, Yusuke Tanaka², Stefano Di Cairano¹ and Dennis Hong²

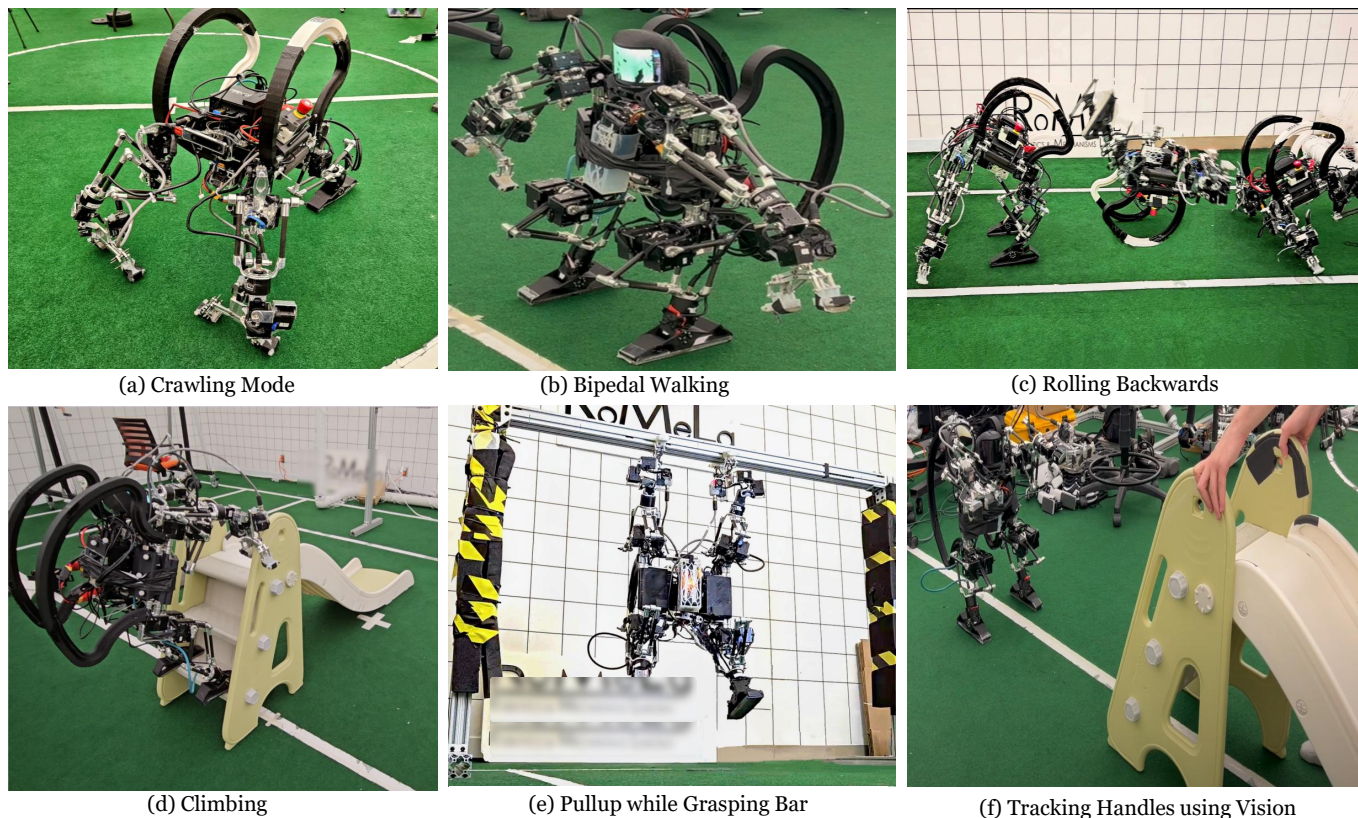


Fig. 1: MOBIUS: Multi-modal Operations Bipedal Intelligent Urban Scout.

Abstract—This article presents a Multi-Modal Bipedal Intelligent Urban Scout robot (MOBIUS) capable of walking, crawling, climbing, and rolling. MOBIUS features four limbs—two 6-DoF arms with two-finger grippers for manipulation and climbing, and two 4-DoF legs for locomotion—enabling smooth transitions across diverse terrains without reconfiguration. A hybrid control architecture combines reinforcement learning-based locomotion with model-based predictive and admittance control enhanced for safety by a Reference Governor toward compliant contact interactions. A high-level MIQCP planner autonomously selects locomotion modes to balance stability and energy efficiency. Hardware experiments demonstrate robust gait transitions, dynamic climbing, and full-body load support via pinch grasp. Overall, MOBIUS demonstrates the importance of tight integration between morphology, high-level planning, and control to enable mobile loco-manipulation and grasping, substantially expanding its interaction capabilities, workspace, and traversability.

I. INTRODUCTION

The advantage of legged robots over other morphologies is their inherent versatility from having multiple degrees of freedom to overcome complex and human-made terrain. This capability provides significant potential for applications such as search and rescue, exploration of extraterrestrial bodies in space [1], delivery [2], and inspection in dangerous areas such as nuclear power plants or failing infrastructures [3]. So far, there have been many different morphologies of legged robots with various types of locomotion abilities. For example, robots capable of bipedal locomotion such as ATLAS [4], Cassie [5], and Digit [6]. Quadrupedal robots such as Unitree [7], [8], ANYmal [9], Cheetah [10], and Spot [11], which work particularly well in rough terrain. And even robots capable of hopping locomotion, such as Raibert’s 3D one-legged hopping machine [12], and the Salto-1P jumping robot [13]. There has also been tremendous progress towards robotic designs that can demonstrate limbs capable of grasping. For example, in [14], all four legs are used to manipulate and balance an object or grasp objects using a dedicated arm [15] or end-effectors [16]. Simultaneous locomotion and grasping, or loco-grasping, enables carrying and using tools while under motion

¹A. Schperberg, and S. Di Cairano are with Mitsubishi Electric Research Laboratories (MERL), Cambridge, MA 02139 USA (email: schperberg@merl.com, dicairano@ieee.org).

²Y. Tanaka, and D. Hong are with the Robotics and Mechanisms Laboratory, Department of Mechanical and Aerospace Engineering, University of California, Los Angeles, CA, 90095, USA (email: dennishong@g.ucla.edu).

[17]. However, only a few robot designs allow for the extreme case of loco-grasping, such as free-climbing [18], facilitating extreme terrain traversal that includes not only continuous environments (e.g., hills) but, importantly, discrete environments (e.g., ladders, climbing holds). This case of free-climbing is essential for highly complex environments such as moving through caves or construction sites. Such free-climbing has been shown using adhesion in [19]–[21]. Still, such adhesive end-effectors are unsuitable for dexterous contacts, limiting their loco-grasping ability. Another method has been through the use of spine-based grippers such as those seen in LEMUR 3 [22] and HubRobo [1], which perform passive grasping [23]. However, both do not demonstrate free climbing under the gravity of Earth [24], which simplifies the climbing task, where dynamic climbing is not necessary to prevent failure cases (e.g. falling). The quadruped SCALER climbing robot [24], [25] addresses loco-grasping challenges under the Earth’s gravity, but it has limited locomotion capability on the ground.

However, many of these robots are still tailored to excel in a specific mode of locomotion, limiting their adaptability across diverse environments. For instance, quadruped robots demonstrate impressive performance on rough, uneven terrain but struggle with discrete structures and vertical surfaces. Conversely, climbing robots can traverse vertical walls with ease, but exhibit reduced efficiency and agility during ground locomotion. Thus, a robot that can change morphology depending on its current environment or task, is a worthwhile endeavor. After all, the ideal robot may be one that can make use of all its limbs to traverse rough and even vertical terrain, perform manipulation through grippers, and employ low-energy efficient motion when possible. Towards this end, we introduce **MOBIUS: Multi-modal Operations Bipedal Intelligent Urban Scout**. MOBIUS is not only capable of dynamic free climbing but can also seamlessly transition between multiple locomotion modes, allowing it to adapt to diverse terrains and perform a wide range of tasks efficiently. For rough terrain, it can make use of its crawling capability, using all four limbs for added stability and robustness. For difficult-to-reach places, such as pushing a button on an elevator, MOBIUS can transition into a bipedal mode, where its forearms are free for manipulation tasks. Equipped with two GOAT [26] grippers, MOBIUS can support its entire body weight. What sets MOBIUS apart is its ability to grasp and pull itself up on bars using a pinching grasp, rather than merely hooking onto them. This demonstrates the strength of its grippers, highlighting the robot’s design and versatile manipulation capabilities. To the best of our knowledge, MOBIUS is the first mid-sized bipedal robot, powered by high-gear ratio position-controlled motors and trained with model-free reinforcement learning, that can both locomote bipedally and support its entire weight with a pinching grasp to achieve all modes of mobility: walking, crawling, climbing, and pull-up.

A. Contributions

Our **contributions** are summarized as follows:

- We present the design of a novel multi-modal robot, featuring two highly dexterous limbs with 6 Degrees of

Freedom (DoF) joints, each equipped with a two-finger gripper [26] to perform grasping and manipulation tasks. The remaining two limbs are optimized for locomotion, consisting of 4 Degrees of Freedom legs with a flat-foot structure to enhance stability during movement. Additionally, rails mounted on the robot’s back serve a dual purpose: providing fall protection and enabling backward rolling for enhanced mobility.

- MOBIUS morphology allows for bipedal, crawling, and rolling locomotion. Using its two longer arms with grippers, it can also achieve vertical free-climbing under the earth’s gravity, such as ladders, and perform pull-ups.
- We extend the admittance controller from [27] to provide safety guarantees through a reference governor.
- A high-level planner is presented to exemplify changing modes depending on the environment using a Mixed Integer Constraint Programming Solver.
- Extensive hardware validation is presented - we show transitions between biped to crawling, crawling to biped, rolling, biped and crawling locomotion, push-ups, and using vision to locate, track, and maneuver the robot to overcome a slide.

B. Paper Organization

The paper is organized as follows. Related works on multi-modal robots, covering both hardware and software aspects, are presented in Sec. II. The MOBIUS hardware is described in Sec. III, including design challenges such as multi-modality requirements, performance–robustness trade-offs, and integration and scalability considerations (Sec. III-A). The mechanical architecture and limb designs are detailed in Sec. III-C, while actuator selection, fatigue analysis, and reliability are discussed in Sec. III-D. The gripper and foot end-effectors are presented in Sec. III-E. The software architecture (Sec. IV, Fig. 6) covers locomotion modes (Sec. III-B), RL-based planning and control (Sec. IV-A), and the model-based MPC baseline (Sec. IV-B). Additional modules include the force controller (Sec. IV-C), state estimator (Sec. IV-D), visual-servo controller (Sec. IV-E), and high-level multimodal planner (Sec. IV-F). Finally, Sec. V presents simulation and hardware integration (Sec. V-A) and extensive experimental results on locomotion, mode transitions, climbing, pull-ups, force control, comparisons between MPC and RL, multimodal planning, and visual-servo tracking.

II. RELATED WORK

We discuss related works from two perspectives. First, focusing on the hardware and design choices to achieve multi-modality (e.g., changing from bipedal to quadruped mode or rolling mode) in Sec. II-A. Second, describing from the perspective of the software architecture, namely planning and control of such multi-modal systems, in Sec. II-B.

A. Hardware for Multi-Modality

The significance of multi-modal robots lies in their adaptability to operate in diverse environments by exploiting multiple locomotion strategies within a unified platform. Several

robotic systems have pursued this objective through morphological or actuation-based innovations. Harpy [28] and LEONARDO [29] are bipedal robots equipped with torso-mounted thrusters that enable transitions between walking and short-duration flight, allowing them to overcome obstacles that would otherwise be impassable for purely legged systems. Modular robots such as AuxBots [30] exemplify volume-changing architectures that achieve flipper-style locomotion through flexible inter-robot connections without relying on rigid lattices. Similarly, origami-inspired modules presented in [31] enable shape morphing and variable stiffness actuation for transitioning between rigid and soft locomotion states.

ALPHRED [32] extends quadrupedal morphology by attaching limbs in a radially symmetric configuration, enlarging its workspace and enabling dual-arm manipulation alongside locomotion. This flexibility allows ALPHRED to perform manipulation tasks, such as picking up a box, while maintaining balance. RiSE [20] adopts a bio-inspired climbing design, utilizing compliant legs and micro-spine feet to adhere to rough surfaces, achieving vertical mobility on surfaces up to 90 degrees. ANYmal-Wheel [33] combines legged walking with torque-controlled wheeled locomotion, enabling smooth transitions between modes and achieving high speed and efficiency. The robot in [34] demonstrates further versatility by incorporating mechanisms that support driving, rolling, and swimming through both active and passive deformation. Similarly, the soft wheel-leg robot [35] integrates pneumatic actuation with wheel-like appendages to traverse constrained or irregular environments by combining rolling, crawling, and bending motions.

While these systems achieve impressive adaptability, they typically require mechanical reconfiguration or rely on appendage-specific mechanisms to transition between locomotion modes, leading to increased complexity and mass. MOBIUS, by contrast, achieves four distinct locomotion modalities—walking, crawling, climbing, and rolling—through a single, unified morphology without any physical reconfiguration. Its limbs, integrated with the GOAT [26] gripper, provide both compliant ground contact and high-force grasping for climbing. This dual-purpose design minimizes hardware redundancy, enabling seamless transitions between locomotion styles while maintaining structural simplicity and robustness. While only a few robots, such as the ARMStrong Dex [36], have demonstrated pull-up capabilities, MOBIUS is the first mid- to large-sized bipedal robot capable of performing a pinch-grasp pull-up starting from a fully extended, dead-hang arm configuration.

B. Multi-Modal Planning and Control

In multi-modal systems, coordinating multiple locomotion strategies requires robust planning and control frameworks that can handle discontinuous dynamics and varied contact conditions. Harpy [28] uses thrusters to regulate ground reaction forces and recover balance during instability, mitigating the need for complex trajectory optimization. AuxBots [30] employ a control architecture that manipulates distances between antipodal points using leadscrews, allowing flipper-style

motions with high energy efficiency. The origami-inspired robot [31] utilizes shape morphing through Variable-Stiffness Joints (VSJs), whose configurations are computed analytically to enable walking, crawling, and grasping through structural reconfiguration.

RiSE [20] coordinates climbing, walking, and surface transitions using a distributed sensing and actuation system, fusing joint position, leg strain, and contact feedback for gait adaptation. ANYmal-Wheel [33] employs a hierarchical whole-body controller (WBC) under a zero-moment-point (ZMP)-based optimization framework, continuously updating wheel and leg trajectories while enforcing nonholonomic rolling constraints. The soft wheel-leg robot [35] synchronizes pneumatic and wheel motions to adapt between gecko-like and inchworm-like crawling strategies depending on terrain.

Beyond mode-specific designs, hybrid approaches such as [37] explore transitions between quadruped and bipedal gaits using Automated Residual Reinforcement Learning (ARRL), a framework that integrates conventional feedback control with model-free reinforcement learning (RL) to improve adaptability and performance across terrains. ARRL leverages off-policy algorithms like Soft Actor-Critic (SAC) and Twin Delayed Deep Deterministic Policy Gradient (TD3) to refine motion policies over time, enabling efficient locomotion in diverse conditions.

Building upon these foundations, MOBIUS introduces a cohesive hybrid control architecture that unifies model-free and model-based paradigms under a shared actuation and sensing framework. Reinforcement learning policies trained in simulation govern bipedal and crawling behaviors, while a model-based baseline controller using Raibert-style gait generation and MPC tracking ensures stability and interpretability across conditions. For contact-intensive tasks such as climbing and pull-ups, MOBIUS employs an admittance-based force controller augmented with a Reference Governor, enforcing safety constraints online. At the high level, MOBIUS autonomously selects optimal locomotion modes using a Mixed-Integer Quadratic Constraint Programming (MIQCP) planner, which minimizes energy consumption while satisfying reachability and terrain constraints.

Through this combination of unified morphology, hybrid learning-based control, and optimization-driven planning, MOBIUS achieves fluid, autonomous transitions across locomotion modes—advancing beyond prior systems that depend on discrete, manually triggered, or reconfiguration-based mode changes.

III. HARDWARE AND SYSTEM MECHANISMS

A. Overall Design Challenges

1) *Multi-Modal Requirements*: MOBIUS is a significant modification on the SCALER [24] robot design to enable new locomotion capabilities. MOBIUS arm and leg designs adopt its 5-bar parallel linkage with a serial wrist and ankle. However, multi-modal locomotion, particularly bipedal walking, requires different kinematics and Jacobian designs. When MOBIUS stands up, the limb kinematics configuration differs from the climbing mode seen in SCALER. The limbs

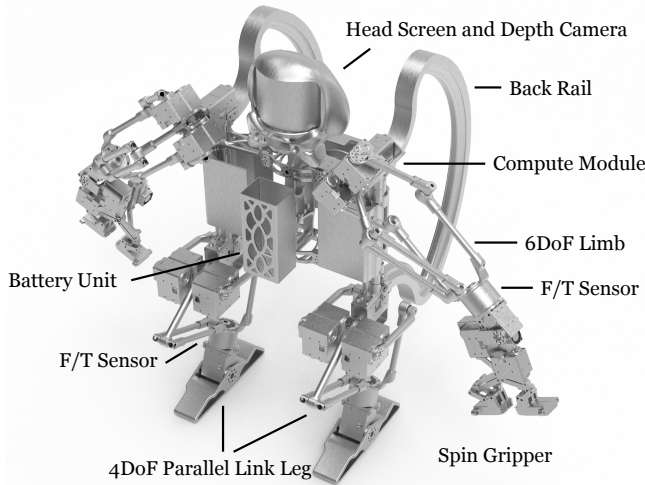
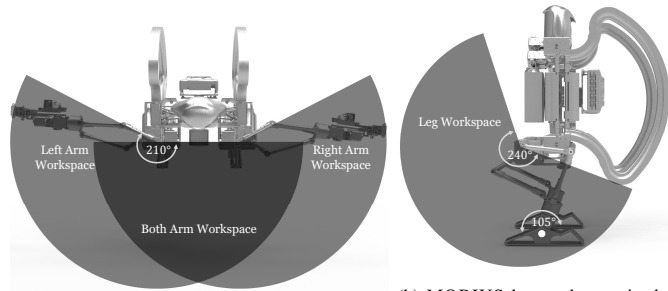


Fig. 2: MOBIUS overall structure rendering.



(a) MOBIUS limb workspace in the top view and with a 210° range. (b) MOBIUS leg workspace in the side view and foot pitch with a 105° range.

Fig. 3: Kinematic ranges of the MOBIUS limb modules.

of MOBIUS are required to support the entire 10 kg robot weight with one leg in bipedal walking, while also being able to lift and swing at an adequate velocity. To enable this functionality, velocity and force ellipsoid design must balance the trade-offs between force exertion and movement speed, particularly at the bipedal and crawling nominal configurations. The arm linkage design is identical to SCALER since it endures less load in crawling motion and does not experience repeated impact when used for climbing. The GOAT gripper must function both as a grasping end-effector for climbing and object manipulation in bipedal mode and as a foot for ground contact in crawling motion. The gripper’s adaptability is crucial for MOBIUS to perform a wide range of locomotion and manipulation tasks seamlessly.

B. Multi-Modalities

The following are the notable locomotion modes that MOBIUS can perform: (1) Bipedal walking, (2) Crawling, (3) Rolling, (4) Vertical mobility, and (5) Mode transitions. A key advantage of this multi-modal capability is that MOBIUS can exhibit versatile directional movement and a broad range of motions, each with different efficiencies. Fig. 4 illustrates MOBIUS’s mobility speed and its range of vertical motion, represented by the maximum height of the trunk pose.

The various modes and capabilities are now discussed in further detail:

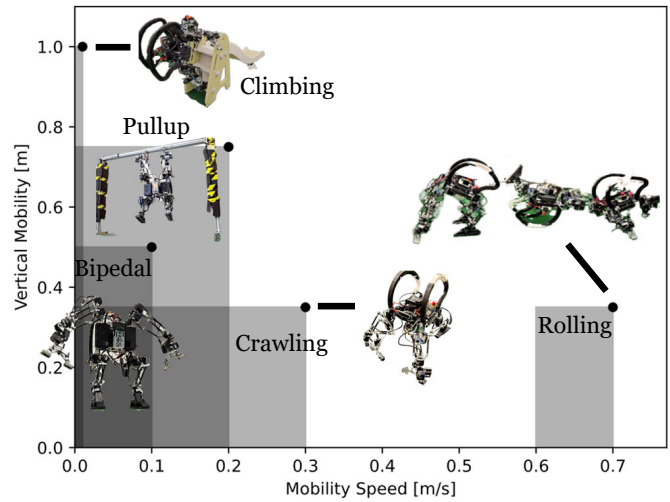


Fig. 4: MOBIUS range diagram. Each mode has various ranges of motion speeds and reachable heights.

1) *Bipedal Locomotion*: Due to the morphology of MOBIUS, the robot is capable of standing on both feet, where its two arms can be used for vertical mobility and/or manipulation tasks. In this mode, the robot is able to stand, walk forwards, backwards, sideways, and also make turns along the yaw rotation. This mode is also used for the visual-servo ability described in Sec. IV-E, which allows it to position its arms such that it can climb the slide shown in (d) of Fig. 1.

2) *Crawling Locomotion*: Due to the flexibility of the goat gripper on the arm, and the large dorsiflexion angle (105° range) capability of the foot ankles, the robot can go on all fours in crawling mode, and walk forwards, backwards, sideways, and rotate along yaw. This mode enables high stability and robustness by utilizing all four limbs to prevent falling, and is particularly beneficial for navigating rough terrain.

3) *Rolling Locomotion*: Due to the back rails attached to the back of MOBIUS, it not only serves as a simple way to avoid damaging the robot when falling backwards, but it is designed to achieve a full 360° backward somersault roll.

4) *Vertical Mobility: Climbing and Pull-Up*: The GOAT [26] grippers, mounted on the limb end-effectors (see Fig. 7), enable the robot to achieve vertical mobility. We demonstrate two examples of this capability: climbing a children’s slide and performing a pull-up under external disturbance.

For the slide-climbing task, as shown in Fig. 14, the robot uses its vision system in conjunction with a simple visual-servo controller (see Sec. 11) to align its end-effectors with the slide’s handle bars. Once aligned, the grippers secure the handle, and the robot coordinates foot placement on each step. By alternating between grasping/releasing the bars and pushing with its feet, the robot can successfully ascend the slide.

The second demonstration involves a pull-up motion using a pinch grasp on an aluminum handle bar, as shown in Fig. 15. When a downward force is applied to the robot, it responds compliantly through force control. Once the disturbance is removed, the robot autonomously pulls itself back up to its

original, undisturbed position, showcasing its adaptability and strength in vertical motion.

5) *Transitions*: The robot is also capable of transitioning between various modes. Specifically, we demonstrate three transition scenarios, illustrated in (A)–(B) and (D) of Fig. 13. In (A), the robot recovers from a front-facing fall by transitioning into crawling mode, with all four limbs contacting the ground. In (B), the robot transitions from a standing posture (two feet on the ground) into crawling mode. Finally, in (D), the robot performs the reverse transition, moving from crawling mode back to biped mode. These offline trajectories are shown on the right side of Fig. 13.

6) *Trade-offs in Performance and Robustness*: MOBIUS must balance the trade-off between force exertion and movement speed, particularly in its bipedal and crawling configurations. To maintain a stable center of mass, the robot’s mass distribution is managed by strategically placing the battery and computing module at the front and rear. For improved postural recovery, curved rails are mounted on the back, as illustrated in Fig. 2. These rails mechanically guide MOBIUS into a posture from which it can stand up, eliminating the need for additional limb workspace at the rear. Ensuring stability across varied terrains and during dynamic maneuvers requires careful actuator selection and structural robustness—especially under high-impact conditions such as those encountered in bipedal locomotion.

C. Mechanical Architecture and Limb Designs

1) *Leg and Limb Kinematics*: MOBIUS’s leg kinematics vary significantly when transitioning between crawling, climbing, and bipedal modes. In bipedal mode, MOBIUS demonstrates a significant advantage in Jacobian design. The velocity ellipsoid volume increased by 19% and became more isometric, as indicated by a 24% reduction in the condition number compared to the SCALER leg parallel linkage. This configuration ensures that the limb lifting and forward swing velocity are nearly isometric, which is ideal for following the cubic trajectory of the bipedal leg swing. Consequently, the force of the ellipsoid shrinks, although the limb can still generate sufficient force. The foot design remains narrow, and since the leg does not have an additional degree of freedom to keep the foot flat with respect to the ground, MOBIUS tends to make line contact on either edge of the foot, particularly when moving sideways.

D. Actuator Selection and Performance

The multi-modality of MOBIUS introduces conflicting design requirements for both limb structure and actuator selection. MOBIUS utilizes high gear ratio spur gears, which, while lightweight and compact, are generally more susceptible to failure compared to planetary or cycloidal gear systems. This vulnerability is especially critical during bipedal locomotion, where repeated impact forces are transmitted to the gearbox, necessitating careful consideration of fatigue failure in the design process. SCALER’s Dynamixel XM-430-350 actuators provided sufficient torque for multi-modal locomotion, but the parallel link driving motors were altered for MOBIUS due to

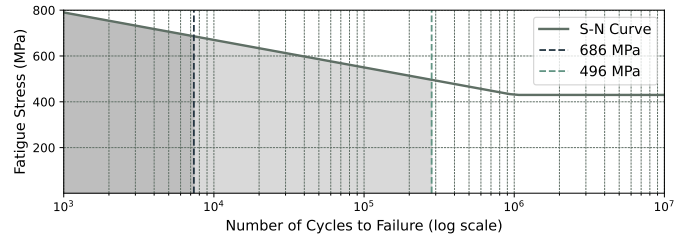


Fig. 5: Fatigue S-N curve for 1045 carbon steel approximated from [41] and the estimated gear teeth strength.

tooth fatigue failure. The 4-DoF leg features a linear, flat foot with a single ankle actuator, while the 6 DoF arm is equipped with the spine-based GOAT gripper [26] and equipped with BOTA F/T sensors at the wrist [38]. The gear bending stress, estimated using AGMA [39], is given by:

$$\sigma_b = \frac{F_t}{mJ} \frac{K_a K_m}{K_v} K_S K_B K_I \quad (1)$$

where σ_b represents bending stress, F_t is the transmitted load per unit width, m is the module, and J is the geometric factor. Given the highly dynamic application, conservative values of $K_a = 2$ and $K_o = 1.5$ were chosen, while other factors were set to 1. At the peak torque observed in bipedal locomotion (2.5 Nm), the estimated bending stress is 496 MPa, with an expected fatigue life of approximately 2.8×10^5 cycles. If the arm parallel linkages and actuators were used for the legs, the gearbox would experience a stress of 986 MPa and failure within 7.2×10^3 cycles due to the smaller module size of 0.4. This fatigue failure difference is visualized in Fig. 5.

Although theoretical calculations predicted a higher fatigue life, experimental results indicated premature failure, likely due to stress concentrations caused by out-of-plane forces. The outer leg linkages exert bending forces on the output shaft, leading to excessive stress concentrations in the gears. To mitigate this, MOBIUS’s legs incorporate additional bearings to isolate stress and maintain uniform loading conditions [40]. Throughout all experiments, MOBIUS’s limbs did not experience gear fatigue, validating the implemented mechanical improvements.

E. End-Effector Design

The multi-modal nature of MOBIUS also presents unique challenges in gripper design. In bipedal scenarios, the arms must function as grasping end-effectors for tasks such as climbing and object manipulation. In contrast, during crawling motion, the same grippers serve as points of ground contact, effectively acting as feet. This dual functionality requires the grippers to be both mechanically robust and versatile to accommodate varying force profiles and interaction modes. The GOAT gripper utilizes finger cells as its foot, with the grasping surface featuring spines. The gripper features a 1-DoF underactuated mechanism for passive adaptability in grasping, which is undesirable when used as a foot. To address this, the GOAT grippers reach singularity when fully closed, eliminating gripper compliance during locomotion. This design enables

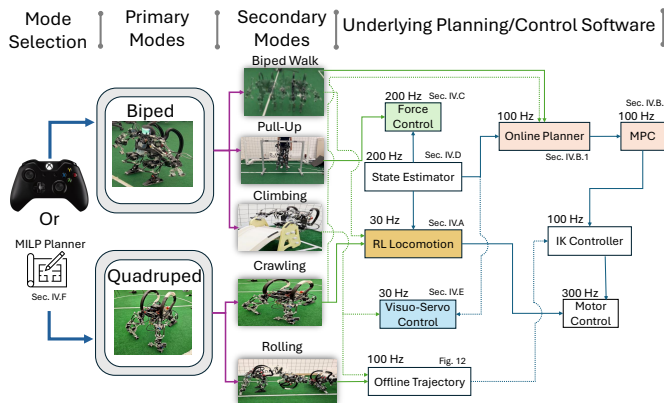


Fig. 6: We demonstrate the overall flowchart, from user primary mode selection, to the secondary modes associated with each primary mode. The modes can be selected either by the user through a joystick, or autonomously (if given a 2D map of the environment with relevant features) using our high level MILP-based planner (see Sec. IV-F). The underlying planners and controllers corresponding to each secondary mode are shown on the right side of the figure, along with their operating frequencies and references to the sections of this work where each module is discussed.

the GOAT gripper to function as both a hand and a foot without requiring additional mechanisms or actuation. Furthermore, the maximum supporting force of the spine-based GOAT gripper on a slippery aluminum bar, as shown in (e) of Fig. 1, demonstrates that the spine generates a shear force of 124.2 N perpendicular to the groove (z-axis), while frictional forces are minimal at 23.6 N parallel to the groove (x-axis). The stochastic nature of the spine contact results in a greater standard deviation of 24.5 N in the z-direction compared to 4.1 N in the x-direction. This indicates that the spine effect dominates the z-direction force components, whereas it cannot generate significant force through pure friction on aluminum in the x-direction. In the z-direction, a single gripper can generate sufficient grasping force to support MOBIUS.

IV. SOFTWARE ARCHITECTURES FOR PLANNING AND CONTROL

The full software architecture and the various locomotion modes are presented in Fig. 6, along with references to the corresponding subsections that provide detailed descriptions which we elaborate here in subsections (A) - (F). Note, that for ablation studies, we compare a reinforcement learning (Sec. IV-A) approach with a model-based approach for biped and crawling locomotion (Sec. IV-B).

A. Reinforcement Learning for Planning and Control

Unlike conventional bipedal and humanoid robots, the forearms of MOBIUS are heavier than its lower body by 55%. While this makes it easier for MOBIUS to switch from biped to crawling mode and vice versa, biped locomotion is particularly challenging not only due to the uneven weight distribution but from the momentum caused by its arms. Although model-based methods are sufficient for most locomotion using more traditional quadruped or biped robots [42]–[46], these methods are insufficient for our particular robot, as the dynamics of MOBIUS are not well understood.

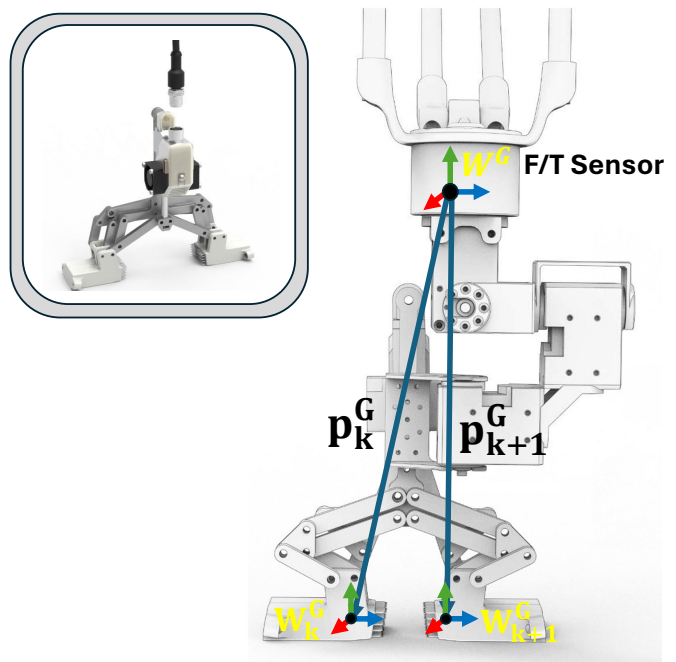


Fig. 7: We provide an illustration of the GOAT [26] gripper, along with our frame definitions of the wrench at the wrist, W_k^G , and the wrenches of the finger tips, W_k^G and their respective positions p_k^G , for finger tip k .

Thus, we opt for a Reinforcement Learning (RL) approach, which has shown significant results in previous works [47]–[52]. However, because of the complexity of our robot model, and unlike the majority of other RL works, we aim to do a completely model-free approach without rewarding the agent based on following some specified trajectory or other type of motion priors [53], [54]. One example of such a model-free approach for bipedal robots was demonstrated on DeepMind’s OP3 humanoid, a small-sized biped [55]. In contrast, we apply this framework to a mid-sized bipedal platform equipped with position-controlled actuators. Learning control policies under position control introduces additional challenges, as the system lacks direct torque authority and must operate through cascaded low-level servos with limited backdrivability and bandwidth. Moreover, the larger mass, inertia, and impact dynamics of a mid-sized robot amplify modeling inaccuracies and contact variability, making stable learning and generalization substantially more difficult compared to smaller, torque-controlled systems.

1) *Problem Definition:* The goal of our RL-agent is to enable the locomotion of MOBIUS to follow user-defined joystick commands – although we show this locomotion in both crawling and biped form, we note that it is the biped form that requires this controller, as crawling mode is stable and can follow user-defined velocities even when using just the model-based approach as outlined in Sec. IV-B. Our RL problem is considered as a Partially Observable Markov Decision (POMDP) Process problem, as we don’t assume access to the full state of our robot/environment. This work will use Proximal Policy Optimization (PPO) as our RL algorithm. Overall, the training procedure is to train the agent on flat terrain first and to use this policy to train again on rough

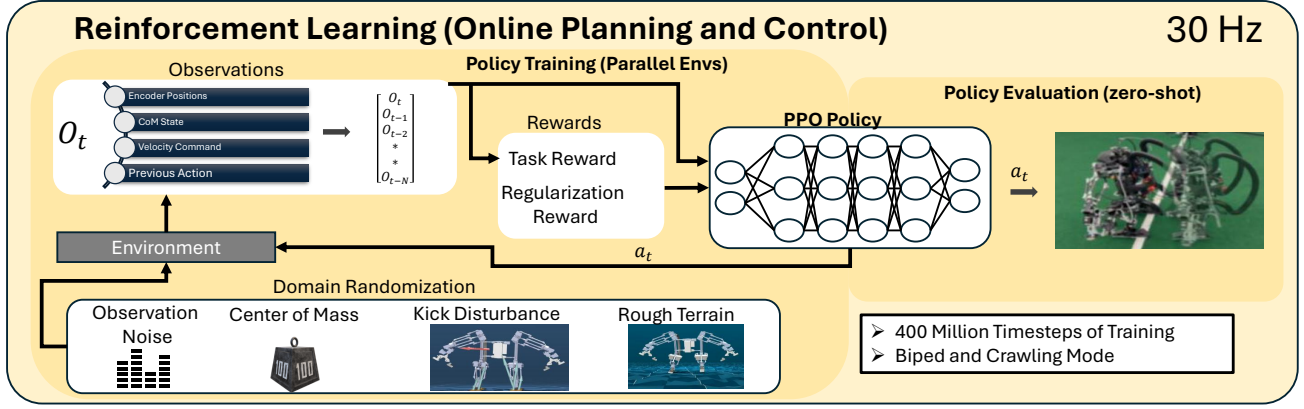


Fig. 8: Our reinforcement learning flowchart is illustrated. It includes the observations used, rewards, and domain randomization, to achieve biped and crawling locomotion as discussed in Sec. IV-A. We trained 300 million time steps on flat terrain, and another 100 million time steps on rough terrain to achieve robustness.

terrain. See Table I for the hyperparameters and number of training time steps used for both flat and rough terrain.

Parameter Name	Value
Mujoco solver time step	0.005
Linear search iteration	3
Constrain iteration	3
Network parameters	(128,128,128,128)
Batch size	256
Learning rate	3e-4
Discounting	0.97
Entropy cost	1e-2
Minibatches	32
Update per batch	4
Num of time steps (flat)	300,000,000
Num of time steps (rough)	100,000,000
Max time step in episode	2000
Max motor RPM	50 (rpm)
Action scale (a_{scale})	0.3

TABLE I: Hyperparameters and settings for RL training

2) *Observation and Action*: The observation space is written as the following: $\mathbf{O}_t = [\mathbf{X}_t, \Theta, \mathbf{A}_{t-1}, \mathbf{v}_{xy}^{des}, \omega_z^{des}, \mathbf{O}_{t-N:t-1}]$, where $\mathbf{X} \in \mathbb{R}^{10}$ is the center of mass of the robot, or the state of the trunk based on state estimation. We consider the orientation in pitch, yaw, and roll, angular velocity in yaw, and linear velocity in x , y , and z , or $\mathbf{X} = [\theta_x, \theta_y, \theta_z, \omega_z, v_x, v_y, v_z]$. $\Theta \in \mathbb{R}^8$ for biped mode or $\Theta \in \mathbb{R}^{14}$ in crawling mode, represents the joint encoder values, and $\mathbf{A} \in \mathbb{R}^8$ for biped mode (4 per leg, for two biped legs) or $\mathbf{A} \in \mathbb{R}^{14}$ for crawling mode (3 per leg for 2 biped legs, as we keep ankle fixed, and 4 per arm for 2 arms, allowing only rotation along yaw for the gripper), and represents the previous actions taken, as defined by equation (2). \mathbf{v}_{xy}^{des} and ω_z^{des} represent the desired trunk linear and angular velocity respectively. Lastly, we consider the history of past observations N , as represented by $\mathbf{O}_{t-N:t-1}$. As we use $N = 15$, our observation space is $\mathbf{O} \in \mathbb{R}^{416}$ in biped mode and $\mathbf{O} \in \mathbb{R}^{608}$ in crawling mode.

$$\Theta_{action} = \Theta_{default} + \left(\frac{1}{n_{actions}} \sum_{i=1}^{n_{actions}} \mathbf{A}_{t-i} \right) a_{scale} \quad (2)$$

where $\Theta_{actions}$ are the joint angles we input to the robot's motors, $\Theta_{default}$ is the starting pose of the robot at initialization, and a_{scale} is a scaling factor. Note, that the term we multiply our scaling factor with is a simple moving average filter (using moving horizon of $n_{actions}$) over the actions received from the RL policy. This is done to provide smoother transitions between actions, which is particularly needed for hardware implementation.

3) *Termination Conditions*: For our RL training procedure, we impose the following termination conditions, which ends the episode:

$$x_z < x_z^{\min} \quad (3)$$

$$\dot{\Theta} > \dot{\Theta}_{\max} \quad (4)$$

$$|\Theta_{action} - \Theta_{limit}| < \epsilon_{limit} \quad (5)$$

$$n_{steps} < n_{limit}^{steps} \quad (6)$$

Where we want to ensure that the episode ends if the current estimated trunk height is below some specified limit (3), the current joint velocities reach beyond the limit set by the maximum RPM from our motors (4), the actions chosen by the policy is near the joint limits by some error ϵ_{limit} (5), or we reach the total number of time steps of our episode given by n_{limit}^{steps} (6).

Reward/Penalty Description	Reward Equation
Penalize Vertical Velocity (R_{v_z})	v_z^2
Penalize Angular Velocity ($R_{\omega_{xy}}$)	$\ \omega_{xy}\ ^2$
Penalize Joint Torques (R_{τ})	$\sum_{i=1}^{N_j} \tau_i \omega_i $
Penalize Change in Actions (R_a)	$\sum_{i=1}^{N_j} (\mathbf{a}_i^j - \mathbf{a}_{i-1}^j)$
Reward Linear Velocity ($R_{v_{xy}}$)	$\exp\left(-\frac{\ \mathbf{v}_{xy}^{des} - \mathbf{v}_{xy}\ ^2}{\sigma}\right)$
Reward Angular Velocity (R_{ω_z})	$\exp\left(-\frac{\ \omega_z^{des} - \omega_z\ ^2}{\sigma}\right)$
Reward Standing Still (R_{stand})	$\sum_{i=1}^{N_j} \theta_i - \theta_i^{ref} (\ \mathbf{v}^{des}\ < 0.1)$
Reward Air Time (R_{air})	$\sum_{i=1}^{N_f} \Delta T_{air} \mathbf{C}_i (\ \mathbf{v}^{des}\ > 0.05)$
Reward Contact ($R_{contact}$)	$\sum_{i=1}^{N_f} \mathbf{C}_i (T_{contact} \geq 0.10)$
Penalize Foot Slip (R_{slip})	$\sum_{i=1}^{N_f} \mathbf{p}_i \mathbf{C}_i ^2 (\ \mathbf{v}^{des}\ > 0.05)$
Penalize Termination (R_{term})	$\text{Done}_{term} (t < 500)$

TABLE II: Reward and penalty formulation for the RL planning and control pipeline.

4) *Reward Function*: For each time step during the training procedure, our RL agent receives rewards or penalties based on the reward function given by Table II. Thus, for stable locomotion, we want to reward/penalize the following: (1) we penalize any vertical velocity, or up and down motion; (2) we penalize the angular velocity in pitch and roll, as we want the body to be upright; (3) we penalize large changes in action to promote smoothness in sequential actions; (4) we reward following a desired linear velocity along the Cartesian plane; (5) we reward the desired angular velocity along the yaw axis; (6) if the desired velocity is near zero, we want to reward the agent for standing still and promote no motion; (7) we reward air time for the feet in motion to promote changes in footstep height and avoid dragging the feet for achieving velocity; (8) we penalize footstep velocities for the feet on the ground to avoid slipping behavior; and (9) we penalize the agent if it does not reach beyond 500 time steps to encourage longevity.

5) *Domain Randomization and Noise*: Employing an RL policy trained in simulation successfully on hardware typically demands sufficient domain randomization [56]–[61]. To this end, we randomize several parameters as shown in Table III. For each time step during training, we add a uniform noise on our state estimate for orientation, angular, and linear velocity. During the reset stage of each episode, we also add uniform noise to the initial starting state of the robot. We also introduce randomness to the observation state of our RL-agent, as shown in Algorithm 1. The objective of this randomization is to simulate potential communication delay of our observations. Additionally, by having a potentially erroneous current observation, the RL-agent may emphasize finding patterns on the change of observations from previous time steps (as our observation space includes a history of N number of past observations). To further robustify against disturbances, we simulate a kick against the robot by adding random linear velocities to the robot’s trunk, \mathbf{v}_{xy} , at every P_{int} number of time steps and at random directions – see Algorithm 2. We also randomize the center of mass and its location, as well as surface friction and actuator gain/bias parameters. Finally, after our agent has finished training on flat terrain, we then continue the agent’s training on a height map to ensure higher success during sim-to-real transfer.

Description	Symbol	Range of Values
Orientation (x, y, z)	θ	$\theta \sim \mathcal{U}(-\pi, \pi)^\circ$
Angular velocity (yaw)	ω_{yaw}	$\omega_{\text{yaw}} \sim \mathcal{U}(-0.15, 0.15)\text{rad/s}$
Linear velocity (x, y, z)	$\mathbf{v}_{\text{linear}}$	$\mathbf{v}_{\text{linear}} \sim \mathcal{U}(-0.05, 0.05)\text{m/s}$
Initial starting state	$\delta\Theta_{\text{default}}$	$\delta\Theta_{\text{default}} \sim \mathcal{U}(0.01, 0.01)^\circ$
Selection of Past Observation	N_{delay}	$N_{\text{delay}} \sim \mathcal{U}(1, 3)$
Prior Selection Chance	p	0.3
Kick Interval	P_{int}	$P_{\text{int}} \sim \mathcal{U}(10, 30)$
Kick angle	θ_{kick}	$\theta_{\text{kick}} \sim \mathcal{U}(0, 2\pi)^\circ$
Body mass	m_{body}	$m_{\text{body}} \sim \mathcal{U}(5.0, 5.0)\text{kg}$
Body location (x, y, z)	\mathbf{l}_{body}	$\mathbf{l}_{\text{body}} \sim \mathcal{U}(-0.1, 0.1)\text{m}$
Surface friction	$\delta\mu$	$\delta\mu \sim \mathcal{U}(-0.3, 0.5)$
Actuator gain	$\delta\mathbf{k}_{\text{act}}$	$\mathbf{k}_{\text{act}} \sim \mathcal{U}(-20, 20)$
Actuator bias	$\delta\mathbf{b}_{\text{act}}$	$\mathbf{b}_{\text{act}} \sim \mathcal{U}(-20, 20)$

TABLE III: Domain randomization parameters.

Algorithm 1 Introduce Randomness in Observations

```

1: Input: Current time step  $t$ , Number of past observations
    $N$ , Max number of delay  $N_{\text{delay}}$ , Probability  $p$  of selecting
   a past observation, Current and past observations  $\mathbf{O}_t =
   [\mathbf{O}_t, \mathbf{O}_{t-1}, \dots, \mathbf{O}_{t-N+1}]$ 
2: Output: Current observation  $\mathbf{O}_{\text{current}}$ 
3: Draw a random number  $r \sim \mathcal{U}(0, 1)$ 
4: if  $r \leq p$  then
5:   Draw a delay  $D \sim \mathcal{U}(1, N_{\text{delay}})$ 
6:   Set  $\mathbf{O}_{\text{current}} \leftarrow \mathbf{O}_{t-D}$ 
7: else
8:   Set  $\mathbf{O}_{\text{current}} \leftarrow \mathbf{O}_t$ 
9: end if
10: return  $\mathbf{O}_{\text{current}}$ 

```

Algorithm 2 Update Velocity with Kick

```

1:  $\theta_{\text{kick}} \sim \mathcal{U}(0, 2\pi)$ 
2:  $\mathbf{k}_{\text{kick}} \leftarrow \begin{bmatrix} \cos(\theta_{\text{kick}}) \\ \sin(\theta_{\text{kick}}) \end{bmatrix}$ 
3:  $\mathbf{k} \leftarrow \mathbf{k}_{\text{kick}} ((n_{\text{steps}} \bmod P_{\text{int}}) == 0)$ 
4:  $\mathbf{v}'_{x,y} \leftarrow \mathbf{v}_{x,y} + \mathbf{k} \cdot \text{kick\_vel}$ 
5:  $\mathbf{v}_{x,y} \leftarrow \mathbf{v}'_{x,y}$ 

```

B. Baseline Locomotion using Model-Predictive Control

The baseline locomotion employs an online planner (Sec. IV-B1) to generate reference trajectories given a desired trunk linear and angular velocity, and which is then tracked by a Model Predictive Controller (MPC) (Sec. IV-B2).

1) *Online Planner*: The first two equations represent the Raibert feedback controllers for the x and y directions:

$$\text{raibert}_x = k_x(\dot{x}_{\text{cur}} - \dot{x}_{\text{des}}) \quad (7)$$

$$\text{raibert}_y = k_y(\dot{y}_{\text{cur}} - \dot{y}_{\text{des}}) \quad (8)$$

These equations calculate the corrective terms, raibert_x and raibert_y , in the x and y directions based on the difference between the current velocity \dot{x}_{cur} , \dot{y}_{cur} and the desired velocity \dot{x}_{des} , \dot{y}_{des} . Here, \dot{x}_{cur} and \dot{y}_{cur} are the current velocities in the x and y directions, while \dot{x}_{des} and \dot{y}_{des} are the desired velocities. The feedback gains k_x and k_y are defined as $k_x = \sqrt{\frac{\bar{p}^z}{g}}$ and $k_y = \sqrt{\frac{\bar{p}^z}{g}}$, where \bar{p}^z represents a reference height or step height and g is the gravitational constant.

The following equation considers the effects of angular velocity on the footstep position in the x and y directions:

$$\begin{bmatrix} \bar{p}_{\text{angular}}^x \\ \bar{p}_{\text{angular}}^y \end{bmatrix} = R(\theta) \begin{bmatrix} \bar{p}^x \\ \bar{p}^y \end{bmatrix} \quad (9)$$

This equation rotates the nominal footstep positions \bar{p}^x and \bar{p}^y by the angle θ , which is related to the desired angular velocity. This accounts for the changes in footstep positions due to body rotation. Here, \bar{p}^x and \bar{p}^y are the nominal footstep positions in the x and y directions, while $\bar{p}_{\text{angular}}^x$ and $\bar{p}_{\text{angular}}^y$ are the adjusted footstep positions accounting for angular velocity.

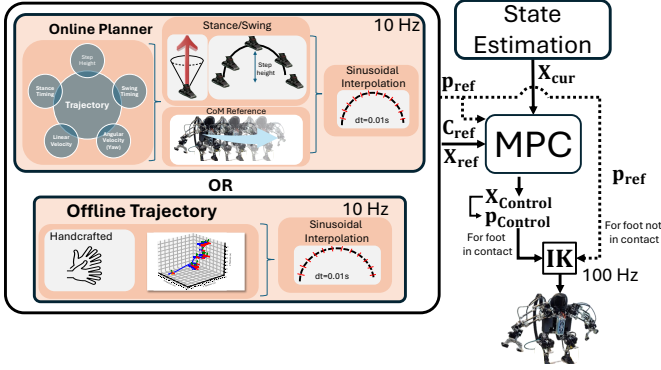


Fig. 9: We show different planning approaches depending on the secondary mode of our robot. For the climbing mode, we hand craft the trajectories offline, and run them primarily open-loop, with some minor correction of grasping hold positioning using the visual-servo controller described in Sec. IV-E. For the locomotion tasks (e.g., biped walking or crawling crawling), we use an online planner to generate trunk and footstep trajectories given a desired trunk linear and angular velocity, and track them via MPC, Sec. IV-B. We compare this model-based method with an RL policy, Sec. IV-A.

The rotation matrix $R(\theta)$ is based on the angle θ , which is calculated as:

$$R(\theta) = \begin{bmatrix} \cos(\theta) & -\sin(\theta) \\ \sin(\theta) & \cos(\theta) \end{bmatrix} \quad (10)$$

with $\theta = \dot{\theta}_{\text{des}} \cdot 0.5 \Delta T$, where $\dot{\theta}_{\text{des}}$ is the desired angular velocity and ΔT is the footstep timing.

The following equations determine the progression terms in the x and y directions:

$$\Delta p_{\text{prog}}^x = \frac{1}{2} \dot{p}^x + p_{\text{angular}}^x + \text{raibert}_x \quad (11)$$

$$\Delta p_{\text{prog}}^y = \frac{1}{2} \dot{p}^y + p_{\text{angular}}^y + \text{raibert}_y \quad (12)$$

These equations calculate the progression terms Δp_{prog}^x and Δp_{prog}^y , which define the adjustment needed in the footstep positions in the x and y directions. They combine the effects of linear velocity, angular velocity, and the Raibert feedback. Here, \dot{p}^x and \dot{p}^y represent the linear velocities in the x and y directions, while p_{angular}^x and p_{angular}^y are the adjusted footstep positions due to angular velocity, and raibert_x and raibert_y are the Raibert feedback terms calculated earlier.

The reference trajectory from the current footstep to the next is generated using a sinusoidal implementation, as detailed in the following equations:

$$\bar{a}_z = p_{\text{step}} \frac{1}{2} \left(\frac{2\pi}{\Delta T} \right)^2 \quad (13a)$$

$$a_{z,t} = \bar{a}_z \cos \left(\frac{2\pi}{\Delta T} t \right) \quad (13b)$$

$$v_{z,t} = \bar{a}_z \frac{\Delta T}{2\pi} \sin \left(\frac{2\pi}{\Delta T} t \right) \quad (13c)$$

$$p_{z,t} = \bar{a}_z \left(\frac{\Delta T}{2\pi} \right)^2 \left(1 - \cos \left(\frac{2\pi}{\Delta T} t \right) \right) \quad (13d)$$

These equations define the vertical motion of the foot using a sinusoidal function. The motion is defined by maximum

acceleration \bar{a}_z , velocity $v_{z,t}$, and position $p_{z,t}$, all functions of time t and step height p_{step} . Here, p_{step} represents the step height, ΔT is the step timing interval, and \bar{a}_z , $a_{z,t}$, $v_{z,t}$, and $p_{z,t}$ are the vertical acceleration, instantaneous acceleration, velocity, and position, respectively.

The equations for horizontal accelerations in the x and y directions are:

$$\bar{a}_x = \Delta p_{\text{prog}}^x \frac{1}{2} \left(\frac{\pi}{\Delta T} \right)^2 \quad (14)$$

$$\bar{a}_y = \Delta p_{\text{prog}}^y \frac{1}{2} \left(\frac{\pi}{\Delta T} \right)^2 \quad (15)$$

These equations determine the maximum horizontal accelerations \bar{a}_x and \bar{a}_y required to achieve the desired footstep positions. Here, Δp_{prog}^x and Δp_{prog}^y are the progression terms calculated earlier.

The horizontal motion of the foot is defined as:

$$a^{xy}(t) = \bar{a}_{xy} \cos \left(\frac{\pi}{\Delta T} t \right), \quad (16)$$

$$v^{xy}(t) = \bar{a}_{xy} \frac{\Delta T}{\pi} \sin \left(\frac{\pi}{\Delta T} t \right), \quad (17)$$

$$p_{xy}(t) = \bar{a}_{xy} \left(\frac{\Delta T}{\pi} \right)^2 \left(1 - \cos \left(\frac{\pi}{\Delta T} t \right) \right). \quad (18)$$

In these equations, $a^{xy}(t)$ and $v^{xy}(t)$ represent the time-dependent acceleration and velocity of the foot in the x and y directions, respectively. $p_{xy}(t)$ indicates the position of the foot. \bar{a}_{xy} is the maximum horizontal acceleration, derived from the progression terms Δp_{prog}^x and Δp_{prog}^y . The motion follows a sinusoidal trajectory to ensure smooth transitions between footsteps.

2) *Model-Predictive Control*: To track the reference trajectories, either from an online planner as proposed in Sec. IV-B1, or from offline trajectories, we employ a Model Predictive Controller (MPC) to calculate the ground reaction forces (for end-effectors in contact with the ground or object) to track the reference trajectory of the body in world frame or $\mathbf{X}_{\text{ref}} \in \mathbb{R}^{12}$, where $\mathbf{X}_{\text{ref}} = [\Theta^\top, \mathbf{r}^\top, \boldsymbol{\omega}^\top, \mathbf{v}^\top]^\top$, Θ is the robot's orientation, \mathbf{r} is the CoM base position, $\boldsymbol{\omega}$ is the angular velocity, and \mathbf{v} is the linear velocity, each with x , y , and z components. While details of this controller can be found in various sources such as [62], [63], because our motors are position-controlled, we employ the approach taken in [24] instead. Specifically, instead of using the ground reaction forces and the inverse Jacobian to calculate the required joint torques, we instead track the ground reaction forces directly using the admittance controller from Sec. 19, which outputs end-effector positions. These end-effector positions can then be converted to desired joint angles through inverse kinematics (see [24]).

C. Grasping Force Control

MOBIUS is capable of lifting its entire weight using its two-finger gripper. However, to ensure that the grasping motion is smooth and safe, not only when trying to achieve its task but also from external disturbances (e.g., pushing

for calculating the MOAS using second-order Euler integration and a control law in Algorithm 3. In summary, we first initialize the position, velocity, and wrench constraints, as well as control gains and discretization parameters. A set of position, velocity, reference position, wrench, and reference wrench grids is then generated to sample system trajectories. The algorithm iterates through each combination of sampled positions, velocities, reference positions, wrenches, and reference wrenches, initializing integral terms and setting a validity flag. Over discrete time steps, the control acceleration is computed and used to update the position and velocity. If any position, velocity, or wrench violates the predefined constraints, the trajectory is deemed invalid and discarded. Otherwise, if the entire trajectory remains within the admissible bounds, the corresponding position, velocity, wrench, and reference values are added to the MOAS set. Finally, the algorithm returns the computed MOAS, which represents the set of all initial conditions that can be controlled while satisfying position, velocity, and wrench constraints. In practice, we apply the MOAS calculation in the x, y, and z-axis for position, velocity, and force, and consider torque along the normal axis with respect to the gripper base.

3) *Employing Reference Governor*: Once we obtain \mathcal{O}_∞ , we can use it to modify (if necessary) the input reference set point, at the current state, such that there exists a feasible control input sequence that ensures output constraints are satisfied over an infinite horizon. To facilitate efficient real-time feasibility checking and control decision-making, we store discrete samples of \mathcal{O}_∞ in a *KD-Tree*, a spatial partitioning data structure that allows for logarithmic-time nearest neighbor search. Given a query state o_q , we can efficiently determine whether $o_q \in \mathcal{O}_\infty$ or, if not, find the closest admissible state $o^* \in \mathcal{O}_\infty$ such that:

$$o^* = \arg \min_{o \in \mathcal{O}_\infty} \|o - o_q\|. \quad (23)$$

In our case, o from equation (23), will be equivalent to $o = [\mathbf{x}, \mathbf{v}, \mathbf{x}_{\text{ref}}, \mathbf{W}, \mathbf{W}_{\text{ref}}]$. Thus, if o is not in the admissible set, o^* is then found by keeping $\mathbf{x}, \mathbf{v}, \mathbf{W}$ constant, and finding the nearest point, in this case, $\mathbf{x}_{\text{ref}}^*$, and $\mathbf{W}_{\text{ref}}^*$, such that it steers the system back into the admissible set.

D. State Estimation

We have two sources of state estimation. The first comes from a T265 IntelRealsense camera, attached to the back of the robot and provides on-board state estimation at 200 Hz using visual-inertial odometry SLAM (i.e., VIO-SLAM). The second source comes from using OptiState [68], which uses a Kalman filter that leverages joint encoder and IMU measurements, enhanced by a single-rigid body model incorporating ground reaction force outputs from convex Model Predictive Control (MPC). The state is further refined using Gated Recurrent Unites, integrating semantic insights and robot height from a Vision Transformer autoencoder applied to depth images using a IntelRealsense D435i camera, attached to the head of the robot. The estimations from the T265 camera and OptiState are fused using a simple complementary filter. Note,

Algorithm 3 MOAS Calculation

- 1: Initialize parameters: $\mathbf{x}_{\min}, \mathbf{x}_{\max}, \mathbf{v}_{\min}, \mathbf{v}_{\max}, \mathbf{w}_{\min}, \mathbf{w}_{\max}, T, dt, N$
- 2: Define control gains: $\mathbf{D}_d, \mathbf{K}_d, \mathbf{K}_f, \mathbf{K}_{I_x}, \mathbf{K}_{I_f}$
- 3: Generate state and reference grids: $\mathbf{x}_{\text{samples}}, \mathbf{v}_{\text{samples}}, \mathbf{x}_{\text{ref_samples}}, \mathbf{W}_{\text{samples}}, \mathbf{W}_{\text{ref_samples}}$
- 4: Create empty list $\mathcal{O}_\infty = []$
- 5: **for** each state $\mathbf{x}_{\text{cur}}, \mathbf{v}_{\text{cur}}, \mathbf{x}_{\text{ref}}, \mathbf{W}_{\text{cur}}, \mathbf{W}_{\text{ref}}$ **do**
- 6: Set valid = **True**
- 7: Set $\mathbf{z}_x = 0, \mathbf{z}_f = 0$ (Reset integral terms)
- 8: **for** each time step $t = 0$ to $T/\delta t$ **do**
- 9: Compute control acceleration \mathbf{u}_t :

$$\mathbf{u}(t) \quad (22)$$
- 10: Update current position and velocity:

$$\mathbf{x}_{\text{cur}} \leftarrow \mathbf{x}_{\text{cur}} + \mathbf{v}_{\text{cur}} \cdot \delta + 0.5 \cdot \mathbf{u}(t) \cdot \delta t^2$$

$$\mathbf{v}_{\text{cur}} \leftarrow \mathbf{v}_{\text{cur}} + \mathbf{u}(t) \cdot \delta t$$
- 11: Check if constraints are satisfied:

if $\mathbf{x}_{\text{cur}} \notin [\mathbf{x}_{\min}, \mathbf{x}_{\max}]$ or $\mathbf{v}_{\text{cur}} \notin [\mathbf{v}_{\min}, \mathbf{v}_{\max}]$,
set valid = **False**
- 12: **if** valid == **False** **then**
- 13: **break**
- 14: **end if**
- 15: **end for**
- 16: **if** valid == **True** **then**
- 17: Add $(\mathbf{x}_{\text{cur}}, \mathbf{v}_{\text{cur}}, \mathbf{W}_{\text{cur}}, \mathbf{x}_{\text{ref}}, \mathbf{W}_{\text{ref}})$ to \mathcal{O}_∞
- 18: **end if**
- 19: **end for**
- 20: **return** \mathcal{O}_∞

the performance of VIO-SLAM from the T265 camera, as well as the details of OptiState are demonstrated in [68].

E. Visual-Servo Controller

The visual-servo component, as shown in Fig. 11, is used primarily for positioning the arms of the robot to grasp the handles of the slide, to help initiate the climbing trajectory. To accomplish this, we first annotate approximately 200 images with bounding boxes for both side handles of the slide. We then train a YOLOv8 [69] model on these annotations. During inference, the bounding boxes of each slide handle and their center positions, or \mathbf{p}^{cam} , are passed into a PID controller running at 300 Hz, with the goal of reducing the error between the current gripper position, \mathbf{p}_{cur} and \mathbf{p}^{cam} . To reduce jerk, and promote smooth motions, we apply a low-pass filter on the output of our PID controller, before running inverse kinematics to pass the joint angles to our actuators. The objective is that distance between the robot's two grippers match the distance of the handle bar slide, and ensuring the gripper center position is centered at the position of \mathbf{p}^{cam} .

F. High-Level Multi-Modal Planning

This section presents a high-level planning framework that enables a multi-modal robot to optimize its trajectory while

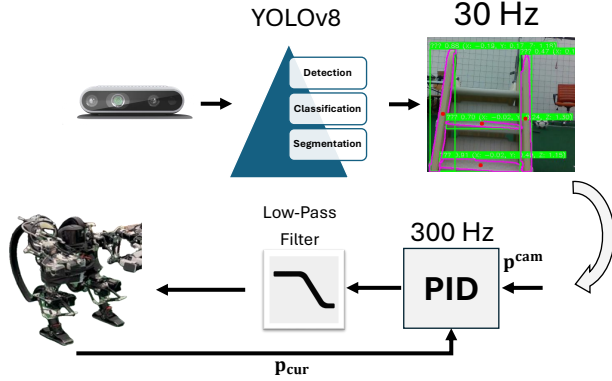


Fig. 11: A visual servo pipeline is used to track the handle bars of a slide before initiating the climbing task. It consists of the YOLOv8 algorithm along with a PID controller for tracking the centroids of the bars (red dots) and low pass filter for smoothness.

dynamically switching between operational modes. Our formulation leverages a Mixed Integer Quadratic Constraint Programming (MIQCP) approach to handle the trade-offs between exploration, goal-reaching, and energy efficiency. In addition, terrain and obstacle constraints are incorporated to ensure safe and feasible navigation.

1) *MIQCP and Mixed Integer Formulation*: A key use case for multi-modal robots is their ability to transition between modes (i.e., crawling, biped, rolling) to meet diverse task requirements. Our framework introduces a high-level task optimization approach specifically designed to leverage this inherent multi-modality. By employing a Mixed Integer Quadratic Constraint Programming (MIQCP) formulation, the planner optimally determines both the robot's trajectory and mode selection, thereby fully exploiting the advanced capabilities of the hardware.

Here, we define the tasks as the robot must navigate from a start to an end goal within a set time frame, avoid obstacles, and maximize exploration of a discretized 2D grid map ($N_{\text{grid}} \times N_{\text{grid}}$ m). This task can be completed with a single mode but with less coverage and efficiency, as discussed later in Sec. V-F.

This grid map is defined by two integer variables, $z(t, i, j)$, which is equal to 1 if the agent visits the grid specified by (i, j) at time t or 0 if not. Using constraints (2), (3), and (4) of Table IV (where T is the total number of time steps permitted) helps define $V(i, j)$ as a binary variable which keeps track of whether a cell is visited or not during the entire time horizon. The path of the robot is represented by continuous variables $x(t, 0)$ for the x -axis and $x(t, 1)$ for y -axis at time step t of the grid map. Constraint (5) and (6) of Table IV ensures that if, for example, $z(t = 5, i = 1, j = 2) = 1$, then we set $x(t = 5, 0) = 1$ and $x(t = 5, 1) = 2$. The big M formulation is used to enforce such conditional constraints (e.g., if and or) for mixed integer problems (see [70]), where M must be set to a high value. Constraint (7) represents the propagation update (we omit x and y for simplicity of notation), where $d(t)$

is a value dependent on the current mode of the agent. The various modes are shown in constraints (8) - (10), where $m_1(t)$ represents biped mode, where the agent can move between -1 to 1 grid cells at a time, $m_2(t)$ represents crawling mode, where the agent can move between -2 to 2 grid cells at a time, and finally $m_3(t)$ represents rolling, where the agent can *only* move at either -3 or 3 grid cells at a time (to simulate that once the robot rolls, it rolls at a fixed distance). Note that the mode variable is binary, and we enforce that the agent can only operate in one mode at any given time using constraint (11). Finally, because during rolling motion the robot state estimation becomes unstable, to simulate this effect, we have added a condition that during this mode, the cells between the start and end of roll are not counted as 'seen.'

2) *Terrain and Obstacle Handling*: To ensure safe navigation, terrain, and obstacle constraints are incorporated into the planning problem. The terrain constraints are modeled as circular regions, as defined by constraints (12) to (15). Constraint (12) calculates the squared distance from the robot's current position to the center of each circle. This distance is then used in constraint (13), where the binary variable b_{circle}^k (with k representing different circles) becomes 1 if the robot is inside the corresponding circle. Conversely, constraint (14) ensures that b_{circle}^k becomes 0 when the robot is outside the circle. A small positive value ϵ is introduced to enforce strict inequality. Constraint (15) links terrain types to the robot's operational modes. For instance, one circular region may represent rough terrain, requiring the robot to operate in crawling mode (i.e., $m_2(t) = 1$). Another circular region might represent an area with elevated objects, such as tables, which the robot can only effectively 'visit' by switching to biped mode (i.e., $m_1(t) = 1$). This reflects real-world scenarios where the robot must stand upright to see or interact with objects placed at a higher level.

Finally, we also ensure that the robot does not enter areas that are considered obstacles, which we represent as rectangles (note, we can also have circular obstacles, but we separate circles and rectangles to make it more clear what is a terrain versus obstacle) in constraints (16) to (20).

3) *Objective functions and Trade-off*: The objective function for this optimization problem is designed to balance two competing goals: maximizing grid exploration and ensuring the robot reaches its target point. The exploration objective is weighted heavily to encourage the robot to visit as many grid cells as possible during its journey. The goal-reaching term penalizes the robot for deviating from the final waypoint position. The overall objective function is a weighted sum of these two components, with the goal of maximizing the sum.

In addition to these two primary terms, a penalty for mode selection is introduced to regulate the robot's movement behavior. Each mode has a different penalty cost associated with it, reflecting the energy expenditure or stability trade-offs involved in using that mode. The penalty weights are assigned as follows: crawling mode carries the lowest penalty as it is more energy-efficient and stable compared to other modes, biped mode has a higher penalty due to the increased instability and energy consumption, and rolling mode carries the highest penalty due to poor localization and a greater risk

of instability.

These penalties discourage the robot from using higher-cost modes unless necessary. The robot will prefer crawling mode as it is the most stable, biped mode when the task requires it, and will resort to rolling mode only when it needs to cover larger distances to satisfy the end-goal requirement within a certain time horizon. This addition ensures that the robot’s movement strategy is both energy-efficient and goal-directed while maintaining stability:

$$\begin{aligned} \max_{V_{i,j,x}} \quad & W_{\text{exp}} \sum_{i=0}^{N_{\text{grid}}-1} \sum_{j=0}^{N_{\text{grid}}-1} V_{i,j} - W_{\text{goal}} \|x_T - x_{\text{goal}}\|^2 \\ & - \sum_{t=0}^{T-1} (P_1 m_1(t) + P_2 m_2(t) + P_3 m_3(t)) \\ \text{s.t.} \quad & (1) - (20), \text{ see Table IV.} \end{aligned}$$

where W_{exp} , W_{goal} are the weights of exploration and goal-oriented task, and P_l for $l = 1, 2, 3$ are weights associated with each mode, penalizing certain modes over others, according to the justification given in Sec. IV-F3.

TABLE IV: MIQCP Constraints (1)-(20)

Visiting Grid Constraints	
(1)	$z(t, i, j) \in \{0, 1\}$
(2)	$z_{\text{sum}}(i, j) = \sum_{t=0}^{T-1} z(t, i, j), \quad \forall i, j \in \{0, 1, \dots, N_{\text{grid}} - 1\}$
(3)	$V(i, j) \leq z_{\text{sum}}(i, j), \quad \forall i, j$
(4)	$V(i, j) \leq T \cdot V(i, j), \quad \forall i, j$
(5)	$x(t, 0) - i \geq -M(1 - z(t, i, j))$
(6)	$x(t, 1) - j \geq -M(1 - z(t, i, j))$
Propagation Update	
(7)	$x(t+1) = x(t) + d(t)$
Mode Types Constraints	
(8)	$m_1(t) = 1 \implies d(t) \in \{-1, 1\}$
(9)	$m_2(t) = 1 \implies d(t) \in \{-2, -1, 1, 2\}$
(10)	$m_3(t) = 1 \implies d(t) \in \{-3, 3\}$
(11)	$m_1(t) + m_2(t) + m_3(t) = 1$
Terrain Type Constraints	
(12)	$d_{\text{circle}} = (x(t, 0) - x_{\text{center}})^2 + (x(t, 1) - y_{\text{center}})^2$
(13)	$d_{\text{circle}} \leq r_{\text{circle}}^2 + M(1 - b_{\text{circle}}^k(t))$
(14)	$d_{\text{circle}} \geq r_{\text{circle}}^2 + \epsilon - M b_{\text{circle}}^k(t)$
(15)	$m_k(t) \geq b_{\text{circle}}^k(t), \quad b_{\text{circle}}^k \in \{0, 1\}$
Obstacle Constraints	
(16)	$x(t, 0) \geq x_{\text{min}} + M(1 - b_1^{\text{rect}}(t+1))$
(17)	$x(t, 0) \leq x_{\text{max}} - M(1 - b_2^{\text{rect}}(t+1))$
(18)	$x(t, 1) \geq y_{\text{min}} + M(1 - b_3^{\text{rect}}(t+1))$
(19)	$x(t, 1) \leq y_{\text{max}} - M(1 - b_4^{\text{rect}}(t+1))$
(20)	$b_1^{\text{rect}} + b_2^{\text{rect}} + b_3^{\text{rect}} + b_4^{\text{rect}} \leq 3$

V. EXPERIMENTAL RESULTS

A. Simulation and Hardware Integration

The simulation-to-hardware integration uses policies trained in the high-fidelity MuJoCo [71] simulation with domain randomization over mass ($\mathcal{U}(5.0, 5.0)$ kg), friction ($\mathcal{U}(-0.3, 0.5)$), actuator gains/biases ($\mathcal{U}(\pm 20)$), and observation delays. RL

TABLE V: Maximum Locomotion Velocities

Name	max (m/s)
Biped Mode	0.1
Crawling Mode	0.4
Rolling Mode	0.7

High-Level Multi-Modal Planner

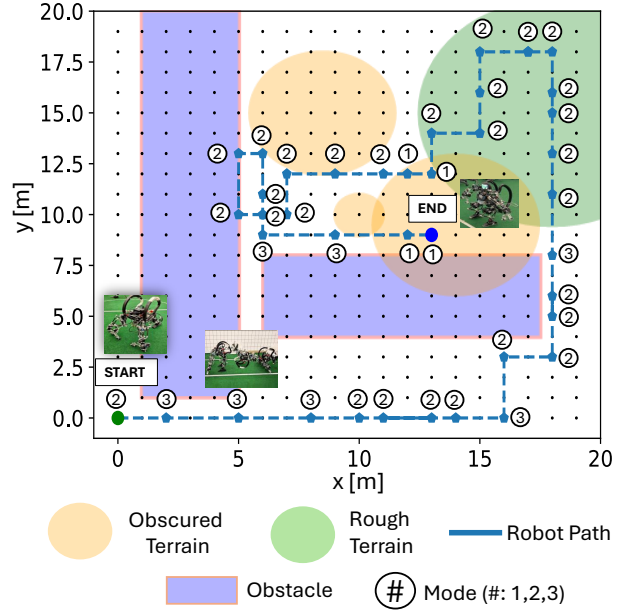


Fig. 12: We show one example map, along with the output of our MIQCP-based planner, where the output consist of connected waypoints, where each waypoint is designated with the desired robot mode selection, numbered from (1) to (3). Mode (1) means the robot must be in biped mode, mode (2) is crawling, and mode (3) is rolling. The solver aims to optimize for reaching the goal or end state within a limited time (or N points), achieve low energy consumption, visit as many cells as possible, avoid obstacles, and meet terrain requirements which may enforce being in one mode or another, see Sec. IV-F.

policies run at 60 Hz, outputting smoothed joint positions via a moving average, tracked by 300 Hz low-level PID motor controllers. For contact-rich tasks like pull-ups, an admittance controller with auto-tuning operates at 300 Hz to ensure compliant force tracking, while safety is enforced using a Reference Governor and a precomputed Maximal Output Admissible Set (MOAS). State estimation fuses the slower T265 VIO-SLAM (200 Hz) with the OptiState algorithm [68] (300 Hz, limited by the computation of our IK), enabling robust real-time control across all locomotion modes with zero-shot sim-to-real transfer. The visual-servo control module enables pre-manipulation positioning by tracking the slide’s handle bars before climbing. An object detection model (YOLOv8) runs at 30 Hz, synchronized with the RGB-D camera, to estimate the centroid positions of the handles. These positions are fed into a PID controller operating at 300 Hz, followed by a low-pass filter to ensure smooth motion. The resulting reference positions are converted to joint angles using IK. For the high-level multi-modal planner, the MIQCP optimization can take approximately 10-11 seconds to solve on a 20 m by 20 m map for a 20 second trajectory. We use Gurobi [72] as the optimization solver. Finally, open loop trajectories run at 300 Hz to match the frequency of our motor controllers.

B. Bipedal Locomotion Performance

We compare a model-based approach, using the online planner and MPC described in Sec. IV-B with the model-free RL approach described in Sec. IV-A for both biped

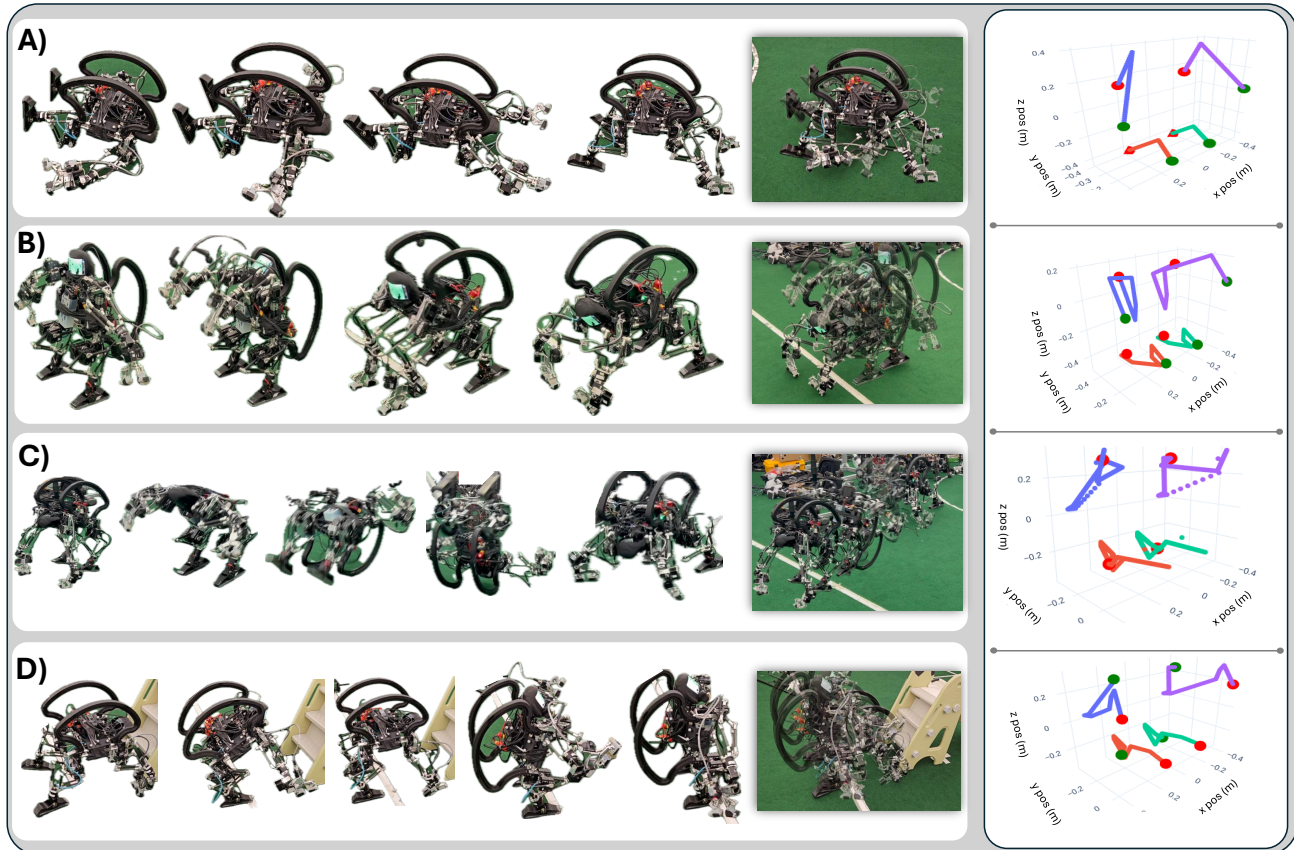


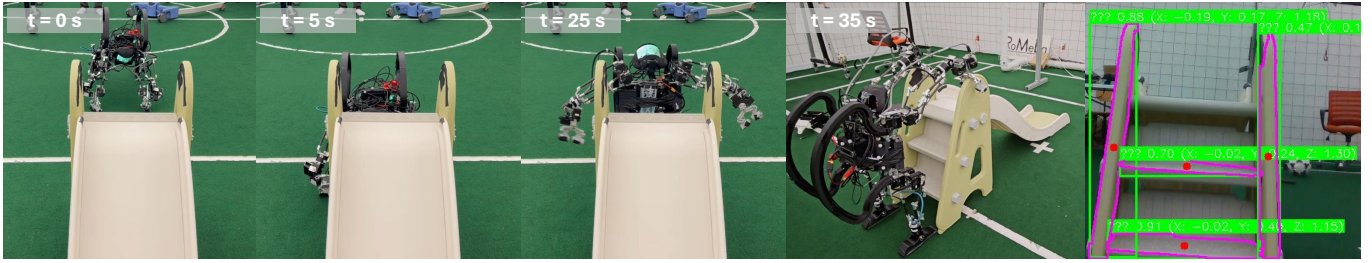
Fig. 13: We present the following motions generated by the offline trajectories visualized on the right of the figure, with limbs that contain grippers in blue and magenta, and limbs with flat-foot end-effectors in red and green. These trajectories include (A) falling to crawling mode; (B) biped to crawling mode; (C) crawling into rolling; and (D) crawling to biped mode.

and crawling locomotion. As biped locomotion is generally challenging and inherently unstable, we demonstrate the robustness of the RL controller over the model-based option in Fig. 16. While we run our controllers during standing, we increase the amount of disturbance through a impulse velocity of 0.1 second duration on the CoM of the robot, where the magnitude (y-axis) is increased over time until the robot falls. As seen in Fig. 16, at about 0.05 m/s of our impulse disturbance, the model-based controller fails, as illustrated by the dashed vertical line. In contrast, the RL policy is able to handle significantly higher disturbance, up to 0.25 m/s, until the policy fails. This result is expected, as MOBIUS exhibits complex, asymmetric dynamics that are difficult to model analytically. These modeling inaccuracies introduce significant errors during the state propagation step of the MPC controller. In contrast, the nonlinear policy learned via RL can implicitly capture these dynamics, resulting in more robust and accurate control. We also were able to validate the RL policy on height map disturbance in simulation, as seen in the bottom right of Fig. 16, as well as hardware experiments as shown in Fig. 1. We further compared our model-based approach with RL for velocity tracking ability in hardware for x , y , and yaw velocities, shown in (A) of Fig. 17, for sideways, forward, backward, and rotation, where green is the target velocity, blue is the estimated velocity for all directional

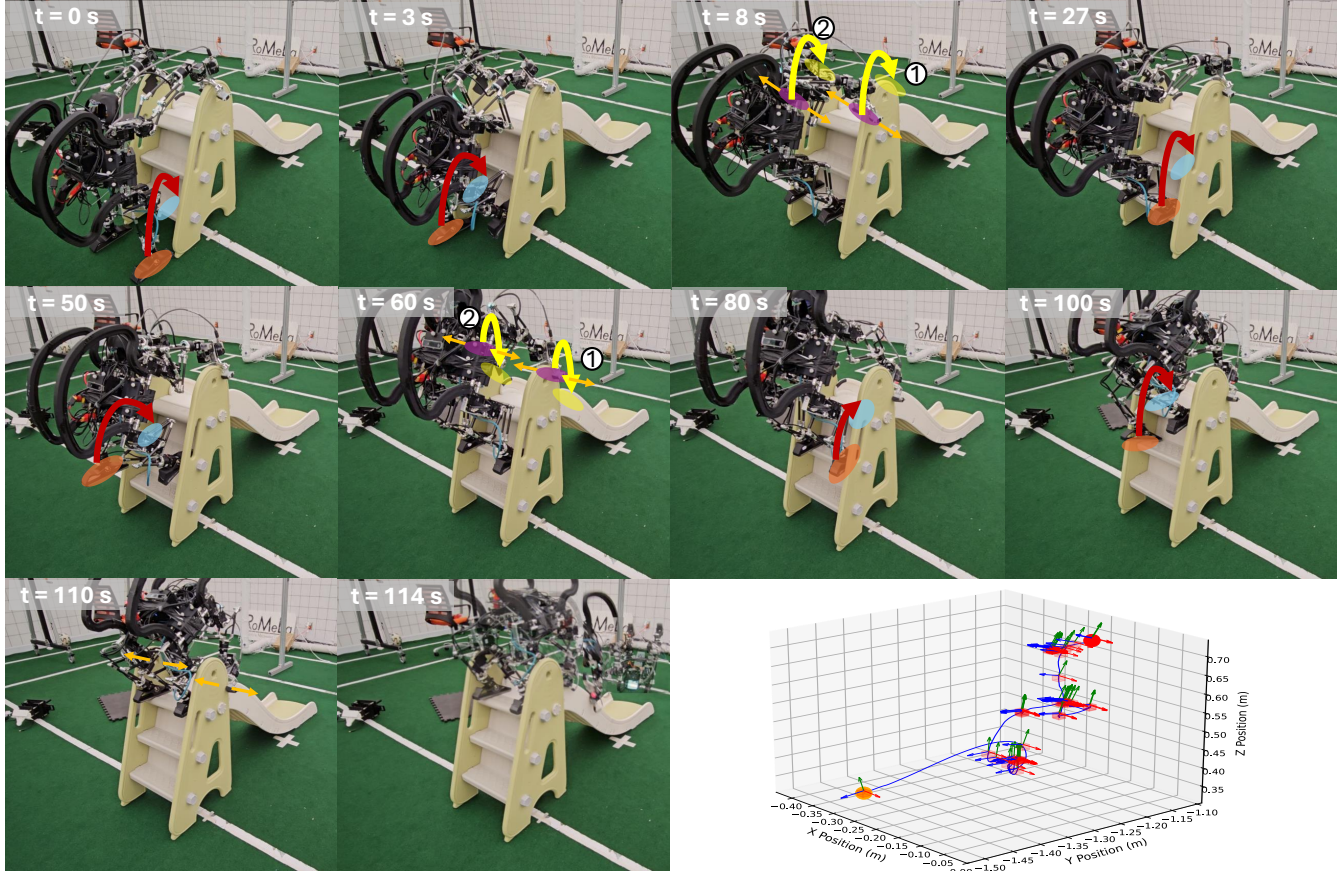
velocity components (using our state estimation pipeline) with our model-based approach, and red is the estimated velocity with our RL policy. Note, our bipedal locomotion can reach up to 0.1 m/s for lateral directions, and 0.25 rad/s in yaw direction. We fill in the curves to visibly show the error of both approaches. As shown, the model-based approach exhibits significantly higher tracking error across all motion types and components. A slight exception appears in forward motion, where the RL policy shows marginally worse performance in tracking the desired x -velocity. However, even in this case, the model-based controller introduces larger errors in undesired directions—specifically in y -velocity and angular velocity—despite these being set to zero during forward locomotion. This suggests the RL policy better suppresses unintended motion while maintaining task-oriented performance.

C. Crawling Locomotion Analysis

A similar velocity tracking comparison between the model-based approach and RL is given for the crawling locomotion in (B) of Fig. 17. Unlike bipedal locomotion, the model-based and RL approach provided more comparable results, although overall, for sideways, and backward motion, RL performed improved tracking. One reason the RL policy struggles with velocity tracking compared to biped locomotion, may be due to the complexity of contact dynamics introduced by using the



(a) Pre-climbing phase: MOBIUS approaches the slide in crawling model, transitions to biped mode, and then uses the visual-servo controller to align its arms with the handle bars. Once aligned, MOBIUS can now initiate the climbing phase, illustrated in (b).



(b) MOBIUS now climbs the stair case, first grasping the top of the handle bars with its arms. It then lifts the right foot and then the left foot to the first step at $t=3$ sec, and releases one arm at a time, so it can grasp further to the handle bar of the slide at $t=8$ sec. The process repeats until at $t=110$ sec, where the robot releases both grippers and naturally can roll down the slide using the back rails to roll down.

Fig. 14: The climbing mode is described in (a) and (b). Where (a) is the pre-climbing phase, and (b) illustrates climbing the slide. In the bottom right figure, we also show a 3D plot of the CoM trajectory of the robot as it goes towards and traverse the slide.

robot's two gripper-equipped arms as front limbs. These grippers were not originally designed for high-frequency ground contact, and the simulator may not accurately model their contact behavior, leading to discrepancies during sim-to-real transfer. Additionally, crawling locomotion operates at higher speeds than biped mode, making tracking more difficult due to increased dynamic effects. Specifically, crawling mode can reach up to 0.4 m/s in lateral directions and 0.6 rad/s in yaw direction. Finally, the asymmetry in limb morphology—two arms and two legs with different masses, kinematics, and end-effectors—introduces further modeling and control challenges not present in more uniform crawling locomotion.

D. Rolling Locomotion

The rolling motion shares similar key points from transition from crawling to standing or biped mode, but before it reaches the default standing pose, it jumps backward and uses the back rail to roll, as shown in (c) of 1. This rolling motion is the fastest locomotion at 0.7 m/s, which is 600.0 % and 133.33 % faster than biped walking and crawling respectively. Nevertheless, although this motion is more energy-efficient compared to biped mode (see Sec. V-E), it is the least stable as the motion cannot be perfectly controlled, particular during the roll where it passively (rather than actively) performs the motion using its back rails. This introduces errors for state

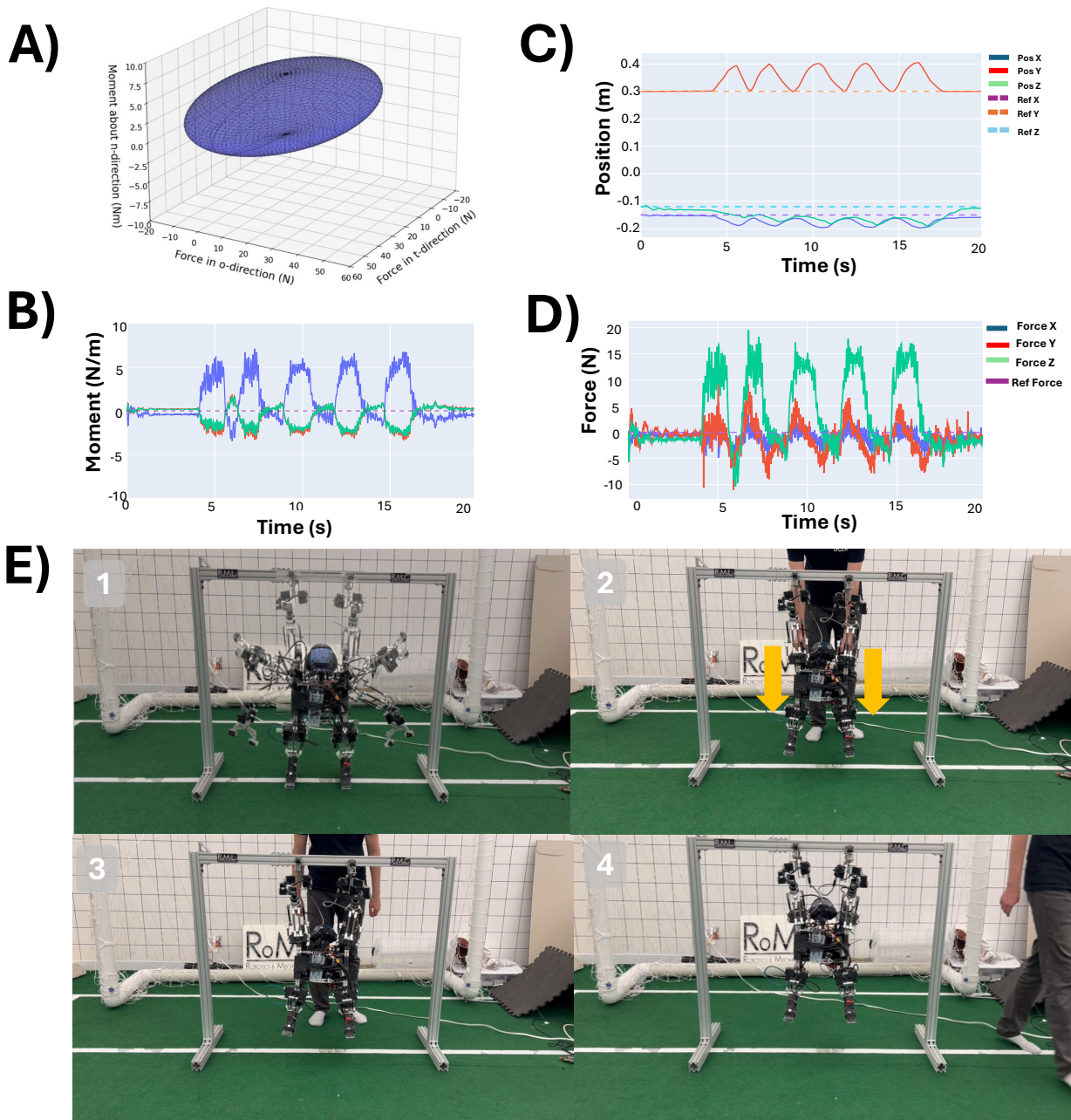


Fig. 15: In (A) we show the force manipulability ellipsoid at the initial grasp position shown in (E)-4 (frame definition given in Fig. 7). The moment about surface normal in (B), position of the end-effector relative to the reference (or initial pose) in (C) given to the admittance controller, and the forces in (D). In (E) we show the entire motion, along with the disturbance from a human pushing the robot downwards as seen in (2).

estimation, where the robot cannot be tracked accurately.

E. Mode Transition: Standup Maneuvers

MOBIUS's standup motions are vital since they are used for transit among modes as well as fall recovery. From the prone pose, i.e., when the robot falls forward in the bipedal mode, MOBIUS can go into the crawling pose using the arms as shown in Fig. 13a. From the crawling to the bipedal mode, MOBIUS uses the arms to lift the body in 13b. However, the arms kinematically cannot reach the ground to push the body completely upward, and thus, the arms are lifted off the

ground to move the center of gravity backward. The simulation in 13c visualizes the change in the center of mass over the corresponding sequence of key points in 13b. In the supine pose, MOBIUS lands on the feet naturally and can stand up without using arms due to the curved back rails. In another case, MOBIUS can land on the head, in which the arms are used to transit to the prone posture instead in the similar way as in the rolling shown in Section. 13c.

Optimal Hyper-Parameter Selection (Top 2) using map from Fig. 12.

W_{exp}	W_{goal}	ϵ	M	T	Comp. Time (s)	Mode Switch Rate	Energy/Visited Cells (J/cell)
20	-20	0.0001	1000	20	10.67	0.27	34.91
200	-200	0.0100	16000	20	11.20	0.22	35.41

Optimal Hyper-Parameter per Mode Selection using simplified version of the map from Fig. 12.

Mode	W_{exp}	W_{goal}	ϵ	M	T	Comp. Time (s)	Energy/Visited Cells (J/cell)	Failure Count
Biped	100	-50	0.001	8000	40	78.86	26.89	270/324
Crawl	50	-1	0.001	8000	20	4.16	5.11	160/324
Roll	1	-1	0.001	8000	15	1.73	21.96	135/324

TABLE VI: Top table shows the optimal parameter selection, from a combination of parameters (324 in total) shown in Table VII, for the top 2 performing combinations using the example map shown in Fig. 12. Performance is evaluated by lowest Energy/Visited Cell. In this test, the planner is able to choose between biped, crawling, and rolling mode. In the bottom table, we remove all terrain from the map, but still include the obstacles. We then force the solver to be either in only Biped, Crawling, or Rolling mode to reach the goal state and show the optimal parameters that achieve the lowest Energy/Visited cell. Note, failure count means how many times the solver failed when exploring the different combination of hyper-parameters per mode.

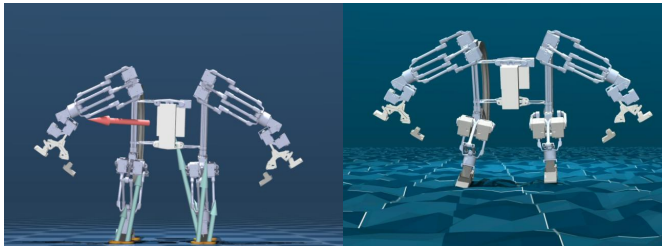
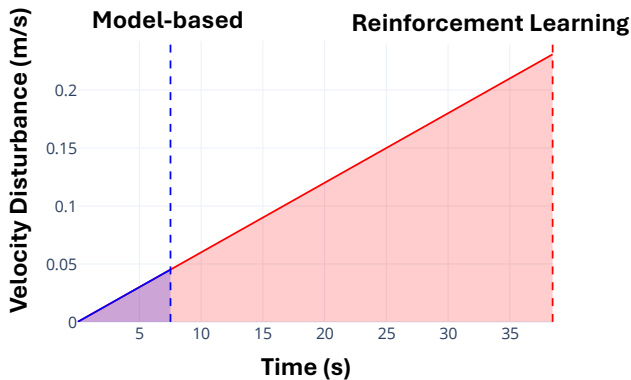


Fig. 16: We compare the model-based baseline approach, Sec. IV-B, with RL, Sec. IV-A, for handling velocity disturbances in the top part of the figure, applied to the base of the robot (red arrow in bottom left figure). The bottom right figure shows the height map environment used to robustify our RL controller.

TABLE VII: Tested Parameter Ranges

Parameter	Tested Values
Weight Exploration	[1, 50, 100]
Weight Goal	[-1, -50, -100]
Small Epsilon	[0.0001, 0.001, 0.01]
M	[1000, 8000, 16000]
T	[10, 15, 20, 40]

F. Multi-Modal High-Level Planning Results

We present the results of our multi-modal high-level planner (Sec. IV-F) in Table VII. The objective of our planner is to reach a goal state, explore the map as thoroughly as possible, while maintaining low energy per visited cell. This metric is calculated by measuring the total energy used—defined as joint velocity multiplied by joint torque—while traversing the

environment, and dividing it by the number of unique grid cells visited. Energy usage is based on each mode’s maximum velocity (see Table V) and the distance traveled in that mode. For example, the crawling mode can move either 1 or 2 cells at a time, with each cell being a 0.5×0.5 meter square. We calculate the energy required to move 1 or 2 cells and divide by the total number of unique cells traversed. The same method applies to biped and rolling modes, with the added constraint that during rolling, the robot must move across 3 cells.

Our first result fixes the total time T while varying all other parameters from Table VII, identifying the two parameter sets that result in the lowest Energy per Grid Coverage while still achieving the goal. These results, using one of our example maps shown in Fig. 12, are listed in the top half of Table IV. The parameters W_{exp} and W_{goal} represent the weights in the objective function that balance exploration and goal-directed behavior. The selection of top-performing hyperparameters was constrained by ensuring the goal was always reached. Additionally, ϵ and M are components of the Big-M inequality constraint, and T denotes the trajectory horizon, defining the total number of allowed time steps. The results indicate that to achieve low Energy per Grid Coverage, a balanced trade-off between exploration and goal-reaching is essential, where ϵ and M are either both low or both high, with an average mode switch rate of around 25% (i.e., the robot switches modes approximately 25% of the time during traversal).

In the bottom half of Table IV, we vary all parameters from Table VII (including T), but constrain the robot to remain in a single locomotion mode throughout the optimization. Here, we aim to find the optimal parameters that lead to the lowest Energy per Grid Coverage while still requiring the robot to reach the goal, necessitating a careful balance of the weights on exploration and on the goal in the objective function. Note that for this test, we do not include mode-specific regions from Fig. 12, only obstacle constraints. The "failure count" column provides further insight into solver performance—out of 324 hyperparameter combinations, it indicates how many resulted in solver failures (due to either poor parameter selection or inability to reach the goal).

Notably, crawling locomotion was the most efficient, achieving the lowest Energy per Grid Coverage of only 5.11 J/cell,

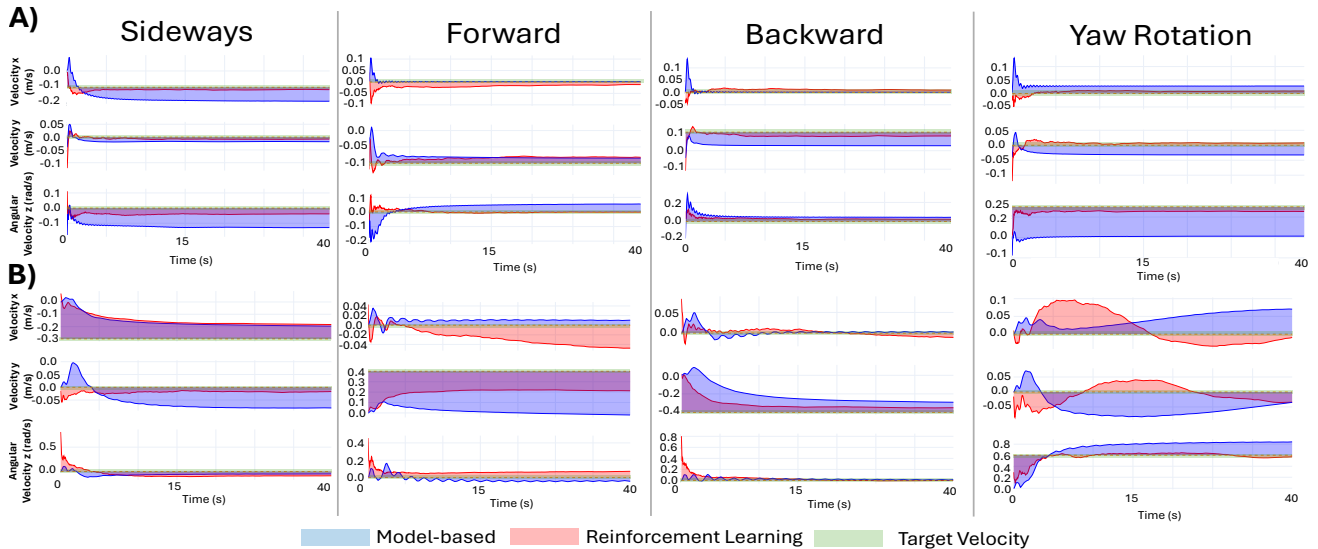


Fig. 17: We compare velocity tracking ability between biped mode shown in row (A) and crawling mode shown in row (B) using the baseline model-based approach, Sec. IV-B and using RL, Sec. IV-A for sideways, forward, backward, and yaw rotation motion. The velocity values for model-based is shown in blue, RL in red, and the target or reference velocity shown in green. For example, in the sideways motion for the biped mode, the target velocity in x is -0.1 m/s, and 0.0 m/s in y and angular velocity (since we command the robot to go sideways only). Note, for our frame definition, the y-axis is pointed forwards.

Locomotion Type	KE (J)	PE (J)	Energy per 1 m (J/m)
Biped	1.35	102.82	104.17
Crawling	6.00	58.86	64.86
Rolling	15.00	0.00	3.00
Pull-up	3.00	58.86	61.86
Climbing	0.60	294.30	294.90

TABLE VIII: Final energy comparison per 1 meter of travel. COM heights: 0.35 m (biped), 0.20 m (crawling). Biped incurs more PE cost due to taller posture, while crawling uses more KE due to greater limb activity. Rolling remains most efficient for horizontal travel.

compared to bipedal at 21.96 J/cell and rolling at 26.89 J/cell. Rolling reached the goal the fastest, requiring only $T = 15$ time steps, which aligns with its inherent speed advantage. However, its effectiveness in grid coverage was lower: during rolling, only a single cell is considered visited due to camera limitations—we impose the constraint that the onboard sensor cannot capture multiple cells while the robot is in fast motion. This constraint was enforced in our MIQCP solver. Biped mode exhibited the highest failure rate, likely because of its limited per-step distance, which requires more time steps T to reach the goal, thereby making it a more difficult optimization problem to solve. Although biped mode may have better grid coverage than rolling, it remains far less energy-efficient compared to the crawling mode. This is attributed to the fact that biped mode covers less distance per step and its motors expend significant energy supporting the full body weight of the robot. Finally, while rolling achieved the fastest traversal, crawling locomotion remains the most effective in terms of Energy per Grid Coverage.

While biped locomotion may appear mechanically simple due to having fewer legs, a closer examination of energy expenditure per meter reveals it is actually less efficient than

crawling locomotion. Using realistic center-of-mass (COM) heights— 0.35 m for biped mode and 0.20 m for crawling mode—we compute that biped mode expends approximately 104 J per meter, compared to only 65 J for crawling. The primary contributor to this difference is potential energy: a biped’s taller posture inherently requires more gravitational work to maintain and move. Furthermore, because bipedal walking demands greater balance and more precise control, the energy load is concentrated over fewer actuators (i.e., two legs instead of four). This results in higher energy usage per leg, which in turn leads to greater motor heating, as more electrical energy is dissipated as thermal loss in each joint. In contrast, crawling distributes both kinetic and control effort across more limbs, reducing peak loads per actuator and improving thermal efficiency. Thus, despite having more limbs in motion, crawling locomotion proves more energy-efficient and thermally manageable than bipedal movement over flat terrain.

G. Vertical Mobility

1) *Vertical Climbing on a Kid’s Slide:* Thanks to MOBIUS’s multi-modal and spine-enhanced GOAT grippers, MOBIUS can climb up a kid’s slide for ages 1-7, shown in Fig. 14. To climb up this slide, MOBIUS has to pinch-grasp the side rails while climbing up on the steps. Once climbed to the top, it slides down from the head. Over the ten trials, eight trials were successful. The two failure cases were caused by a foot failing to progress to the next step, such as the toe getting trapped at the bottom of the step. For this task, we used the visual-servo controller to align the end-effectors of MOBIUS towards the two vertical handles of the slide (see Fig. 14a). After the alignment, we generated an open-loop trajectory for surmounting and then rolling down the slide as seen in Fig.

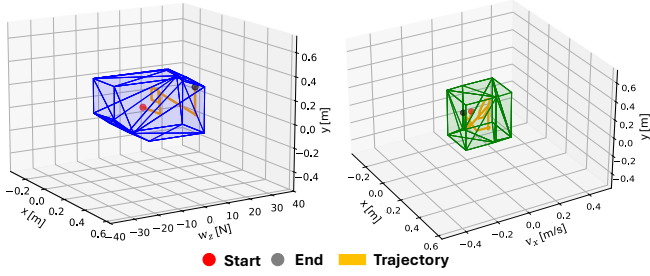


Fig. 18: Example visual representation of the Maximal Output Admissible Set (MOAS), Sec. IV-C1. The trajectory on the left figure represents a 3D state from state estimation following the reference in Fig. 19, where x and y is the end-effector position, w_z is the wrench, and v_x is the linear velocity.

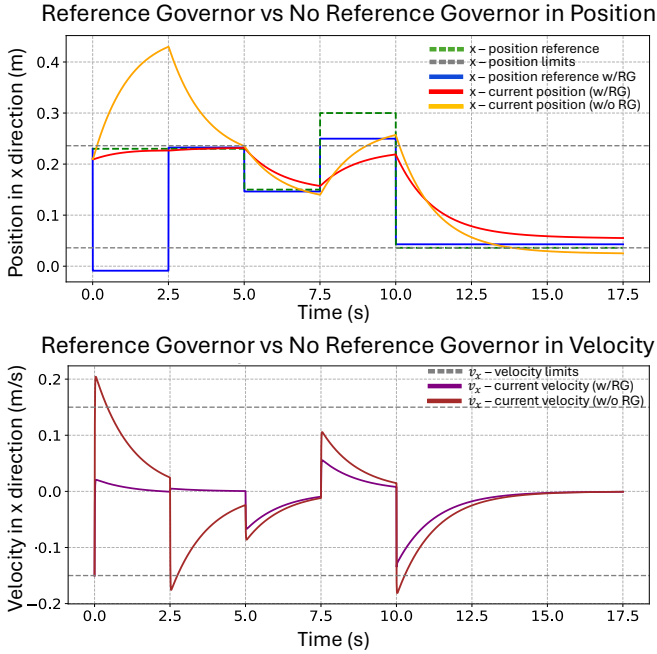


Fig. 19: We compare the results of our admittance controller in tracking a end-effector position (in x) and zero wrench, with and without a reference governor. The constraints for position (top) and velocity (bottom) are marked by dashed lines.

14, demonstrating the capability of the hardware even without closed-loop control.

2) *Pinch Grasp Pull-up*: The pinch grasp and pull-up tasks illustrate the capabilities of MOBIUS’s forearm and gripper mechanisms, as shown in Fig. 15. In this task, MOBIUS uses the GOAT gripper to pinch-grasp aluminum structural bars and then pull-up its entire body from a straight arm dead hang initial position. The uniform design of MOBIUS’s limbs supports the robot effectively, which is particularly advantageous in climbing scenarios. While in the air, the forearm employs admittance control, allowing compliant motion during pullup.

3) *The Maximum Supporting Force of the Spine Contact on the Aluminum Bar*: Typically, spine tips are used on rough surfaces like rock and concrete, which have microcavities. In the pull-up scenario in Fig. 15, the spine tips support the robot’s weight while executing admittance control. The spine inserts into grooves on the aluminum bar, parallel to the bar, as pictured in [24]. These contact dynamics creates a unique limit

surface, representing the boundary of the maximum supporting force of the grasping shown in Table IX. The spine generates a significant shear force of 124.2 N perpendicular to the groove (z -axis), while frictional forces are minimal at 23.6 N parallel to the groove (x -axis). Although the limit surface for the spines is stochastic [26], there is a greater standard deviation of 24.5 N in the z -axis limit compared to that of 4.1 N in the x -axis. This indicates that the spine effect dominates in the z directional force components, whereas the spine cannot generate a significant force with pure friction on aluminum in the x direction. In the z direction, one gripper can generate sufficient grasping force to support MOBIUS.

TABLE IX: Maximum supporting force of the spined GOAT gripper on a slippery aluminum bar in Fig. 15.

Pull Direction	Maximum Supporting Force (Mean)	Uncertainty
x -axis direction	23.6 N	± 4.1 N
z -axis direction	124.2 N	± 24.5 N

4) Auto-Tuning Admittance Control and Safety Analysis:

Manually tuning the admittance force controller for the pull-up was challenging due to the constraints on the two end effectors and the arms bearing the robot’s full weight. The failure case depicted in the accompanied video highlights this difficulty, where each arm and force controller pull against each other, resulting in instability of both the body and the grasp. The auto-tuning improved the force tracking error by 45% while evaluating and maintaining the controller stability. These results match from the expected improvement shown in [27].

In Fig. 15a, we present the force manipulability ellipsoid of the robot arm at the initial grasp configuration, corresponding to the hanging phase depicted in panel 3 of (E). This ellipsoid, defined in task space, spans three axes: torque about the surface normal (z -axis), pulling force perpendicular to the surface (x -axis), and tangential force along the handle (y -axis). It characterizes the set of wrenches (forces and moments) that the end-effector can produce under unit joint torques. The pronounced elongation of the ellipsoid along the x -axis indicates a high capability to generate pulling forces—critical for initiating and sustaining upward motion during climbing. In contrast, the shorter extent along the z -axis reflects a reduced ability to apply torque about the surface normal. This geometry reveals that the arm’s configuration is optimized for exerting strong pulling forces rather than rotational control, aligning well with the functional requirements of the climbing maneuver. Figs. 15b-d show the end-effector wrench and position response during the pull-up maneuver illustrated in Fig. 15e. Specifically, Fig. 15b plots the moment about the gripper normal (z -axis), which varies from approximately -3 N m to 5 N m, while moments in the orthogonal axes remain near zero. Fig. 15c shows the end-effector Cartesian position with reference trajectories: 0.3 m in y (vertical), -0.15 m in x , and -0.12 m in z . The y -axis exhibits a characteristic down-up motion as the robot is first pushed downwards by an external force, and then actively pulls itself upward, returning to the target pose. A small offset in z is also observed, caused by the admittance controller balancing between position tracking

and a zero-force command along that axis, which it cannot satisfy simultaneously. Fig. 15d plots the end-effector forces, where the external disturbance manifests as a downward force of approximately 15 N in y . As the robot completes the pull-up and stabilizes at the reference position, the measured force in all directions approaches zero. This experiment highlights the robot’s ability to absorb external perturbations through passive compliance and then execute a coordinated whole-body recovery using force-aware position control.

We employ the Reference Governor (RG) described in Sec. IV-C1 to provide safety guarantees during force control. We illustrate such safety guarantees in Figs. 18 and 19. In Fig. 18 we show the MOAS set during force control, by tracking the position shown in Fig. 19, with reference wrench set to 0 N. The start of tracking is shown by the red dot, and the end of tracking by a gray dot. The yellow line represents the states from start to end, which is always within the admissible set, demonstrating that our controller can guarantee safety. The effect of RG in providing safety is shown in Fig. 19. We show the x position of the end-effector (red with RG, and yellow without RG), along with the reference position (green dashed), and kinematic limits on x (grey dashed). Without RG, we see that the yellow curve violates the kinematic constraint. With RG, the reference is modified (blue), which enforces the position in x (red) to be within the kinematic limits. Note, that for example from 10.0 to 17.5 seconds, the reference is nearly unchanged by the RG, this is because at this time interval, following the intended reference trajectory leads to the end-effector position to be within the MOAS set (thus, no modification of the reference is required). The bottom graph shows how modifying the reference through RG, also leads the current velocity of the end-effector (purple) to be within the velocity constraints (grey dashed). In contrast, without modifying the original reference trajectory, at times 0.0 sec and 2.5 sec, the current velocity (dark red) violates these limits.

5) *Visual Servoing for Kids Slide*: In Fig. 20, we show the pre-manipulation phase, where the robot has already transitioned into biped mode and must actively position its grippers at the center point of the ladder bar (left and right ladder handles). The bounding boxes (green) and the left and right center points from the handle segmentation (in purple) are obtained using YOLOV8. These handle center points serve as reference targets for the end-effector gripper positions. A PID controller, combined with a low-pass filter for smoother control, is used to track these references, as illustrated in Fig. 11.

To demonstrate the robustness of the controller, we manually moved the slide back and forth. The centroid positions from the vision pipeline are shown in green for the right ladder handle and in blue for the left ladder handle. The measured end-effector positions, computed using joint angles and forward kinematics, are shown in purple for limb 0 (right arm) and orange for limb 3 (left arm). As observed, the end-effectors were able to track the ladder handles even under external disturbances. Notably, large disturbance spikes—such as the one shown in green at approximately 1.2 seconds—were successfully suppressed due to the low-pass filter.

On average, response time during rise (going from 10 % to

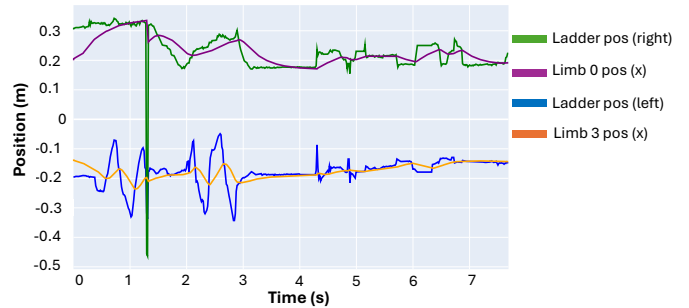


Fig. 20: Example results of the visual-servo controller described in Sec. IV-E. Ladder pos is the centroid position marked by the red dot for the right and left ladder handles respectively. Limb 0 and Limb 1 are the left and right end-effector gripper positions (using x -axis as example).

approx. 90 %) is ≈ 0.5 seconds, and settling time is about 1.75 seconds, which is confirmed by calculating a damping ratio of 0.7 (calculated using our PID parameters, where $K_p = 3.0$, $K_i = 4.5$, and $K_d = 1.0$). Note, that these response times are naturally also affected by the values set by the low-pass filter, which we purposefully calibrated to encourage smoothness (i.e., non-jerky movements) over perfect tracking a moving reference and fast response times, as our objective is to track a largely stationary object.

VI. CONCLUSION

Overall, we showed that MOBIUS is capable of bipedal, crawling, and rolling locomotion, as well as dynamic climbing and pull-up through pinching-based grasping. Our work introduces a unified hardware and software architecture that enables seamless transitions between locomotion and manipulation.

On the hardware side, we demonstrated a compact, fatigue-resistant design combining high-DoF limbs for manipulation and legs for walking and standing, enabling robust interactions in diverse environments. On the software side, we integrated model-free reinforcement learning, model-based planning, admittance force control, and MIQCP-based high-level decision making into a cohesive control stack that adapts to both structured and unstructured tasks.

We validated MOBIUS extensively in both simulation and in hardware, showcasing its ability to perform complex multi-stage tasks such as stand-up recovery, dynamic climbing, and pull-up maneuvers using pinching grasp — the first of its

kind for a biped robot. Our results highlight the importance of tight coupling between morphology, control, and planning in achieving general-purpose mobile loco-manipulation and/or grasping.

A. Limitations

While MOBIUS demonstrates significant advancements in multi-modal robotics—combining bipedal, crawling, rolling, and climbing capabilities within a single platform—several limitations remain.

Hardware Design Trade-offs: The robot’s multifunctional design necessitates compromises. The GOAT grippers serve as both grasping hands and locomotion feet, requiring a balance between compliance and rigidity. This duality increases mechanical complexity and may contribute to long-term wear. Additionally, the reliance on spur gears, while efficient and lightweight, exposes the system to fatigue under the high-impact loads encountered during bipedal locomotion.

RL Control Generalization and Transferability: The reinforcement learning-based control architecture enables robust and adaptive behaviors but is dependent on extensive domain randomization and environment-specific training. These policies may lack generalization to other surface types such as soft or wet surfaces.

Sensing and Perception Constraints: The visual servoing framework relies heavily on YOLOv8 for object detection. Performance can degrade in challenging visual conditions, such as poor lighting or occlusion, which are common in unstructured environments. Furthermore, while state estimation is improved via fusion of visual-inertial odometry (T265) and OptiState, performance may deteriorate during high-speed maneuvers or rolling, when sensor drift and feature loss become more prevalent.

High-Level Planning Reactivity: The MIQCP-based planner effectively optimizes locomotion mode sequences and energy usage but operates offline and lacks the ability to replan in real-time. This limits responsiveness to unexpected environmental changes, such as moving obstacles or terrain deformation. Additionally, in this work, we assume the map and terrain classification was given beforehand.

Energy Efficiency and Mechanical Load: Although the high-level planner incorporates energy-aware objectives, locomotion efficiency varies widely between modes. Bipedal locomotion in particular is both energy-intensive and mechanically taxing on the arm joints. Long-duration missions may require further hardware refinement and adaptive planning to reduce energy expenditure and actuator stress.

In future work, we aim to explore long-horizon autonomy in cluttered environments, leverage language-conditioned control for higher-level task specification, and extend our design for outdoor field deployment.

REFERENCES

- [1] K. Uno, N. Takada, T. Okawara, K. Haji, A. Candolat, W. F. R. Ribeiro, K. Nagaoka, and K. Yoshida, “Hubrobo: A lightweight multi-limbed climbing robot for exploration in challenging terrain,” in *2020 IEEE-RAS 20th International Conference on Humanoid Robots (Humanoids)*, 2021, pp. 209–215.
- [2] G. I. Fernandez, H. Nam, R. Hou, K. Gillespie, and D. W. Hong, “Self-aligning rotational latching mechanisms: A framework extension for orientations & fast latching,” in *2024 6th International Conference on Reconfigurable Mechanisms and Robots (ReMAR)*, 2024, pp. 417–424.
- [3] T. Felsch, G. Strauss, C. Perez, J. M. Rego, I. Maurtua, L. Susperregi, and J. R. Rodríguez, “Robotized inspection of vertical structures of a solar power plant using ndt techniques,” *Robotics*, vol. 4, no. 2, pp. 103–119, 2015. [Online]. Available: <https://www.mdpi.com/2218-6581/4/2/103>
- [4] S. Feng, X. Xinjilefu, C. G. Atkeson, and J. Kim, “Optimization based controller design and implementation for the atlas robot in the darpa robotics challenge finals,” in *2015 IEEE-RAS 15th International Conference on Humanoid Robots (Humanoids)*, 2015, pp. 1028–1035.
- [5] Y. Gong, R. Hartley, X. Da, A. Hereid, O. Harib, J.-K. Huang, and J. Grizzle, “Feedback control of a cassie bipedal robot: Walking, standing, and riding a segway,” in *2019 American Control Conference (ACC)*, 2019, pp. 4559–4566.
- [6] G. A. Castillo, B. Weng, W. Zhang, and A. Hereid, “Robust feedback motion policy design using reinforcement learning on a 3d digit bipedal robot,” in *2021 IEEE/RSJ International Conference on Intelligent Robots and Systems (IROS)*, 2021, pp. 5136–5143.
- [7] G. Bellegarda, Y. Chen, Z. Liu, and Q. Nguyen, “Robust high-speed running for quadruped robots via deep reinforcement learning,” in *2022 IEEE/RSJ International Conference on Intelligent Robots and Systems (IROS)*, 2022, pp. 10 364–10 370.
- [8] A. Schperberg, M. Menner, and S. D. Cairano, “Energy-efficient motion planner for legged robots,” 2025. [Online]. Available: <https://arxiv.org/abs/2503.06050>
- [9] M. Hutter, C. Gehring, D. Jud, A. Lauber, C. D. Bellicoso, V. Tsounis, J. Hwangbo, K. Bodie, P. Fankhauser, M. Bloesch *et al.*, “Anymal—a highly mobile and dynamic quadrupedal robot,” in *2016 IEEE/RSJ international conference on intelligent robots and systems*. IEEE, 2016, pp. 38–44.
- [10] S. Seok, A. Wang, M. Y. Chuah, D. Otten, J. Lang, and S. Kim, “Design principles for highly efficient quadrupeds and implementation on the mit cheetah robot,” in *2013 IEEE International Conference on Robotics and Automation*. IEEE, 2013, pp. 3307–3312.
- [11] A. Bouman, M. F. Ginting, N. Alatur, M. Palieri, D. D. Fan, T. Touma, T. Pailevanian, S.-K. Kim, K. Otsu, J. Burdick, and A.-a. Agha-Mohammadi, “Autonomous spot: Long-range autonomous exploration of extreme environments with legged locomotion,” in *2020 IEEE/RSJ International Conference on Intelligent Robots and Systems (IROS)*, 2020, pp. 2518–2525.
- [12] M. H. Raibert, J. H. Benjamin Brown, and M. Chepponis, “Experiments in balance with a 3d one-legged hopping machine,” *The International Journal of Robotics Research*, vol. 3, no. 2, pp. 75–92, 1984. [Online]. Available: <https://doi.org/10.1177/027836498400300207>
- [13] J. K. Yim and R. S. Fearing, “Precision jumping limits from flight-phase control in salto-1p,” pp. 2229–2236, 2018.
- [14] F. Shi, T. Homberger, J. Lee, T. Miki, M. Zhao, F. Farshidian, K. Okada, M. Inaba, and M. Hutter, “Circus anymal: A quadruped learning dexterous manipulation with its limbs,” in *2021 IEEE International Conference on Robotics and Automation*. IEEE, 2021, pp. 2316–2323.
- [15] Z. Fu, X. Cheng, and D. Pathak, “Deep whole-body control: learning a unified policy for manipulation and locomotion,” in *Conference on Robot Learning*. PMLR, 2023, pp. 138–149.
- [16] M. Su, Y. Qiu, Y. Guan, H. Zhu, and Z. Liu, “Climbot-Ω: A soft robot with novel grippers and rigid-compliantly constrained body for climbing on various poles,” in *2021 IEEE/RSJ International Conference on Intelligent Robots and Systems*. IEEE, 2021, pp. 4975–4981.
- [17] Y. Gong, G. Sun, A. Nair, A. Bidwai, R. CS, J. Grezmaek, G. Sartoretto, and K. A. Daltorio, “Legged robots for object manipulation: A review,” *Frontiers in Mechanical Engineering*, vol. 9, 2023.
- [18] T. Bretl, “Motion planning of multi-limbed robots subject to equilibrium constraints: The free-climbing robot problem,” *The International Journal of Robotics Research*, vol. 25, no. 4, pp. 317–342, 2006.
- [19] S. Kim, M. Spenko, S. Trujillo, B. Heyneman, D. Santos, and M. R. Cutkosky, “Smooth vertical surface climbing with directional adhesion,” *IEEE Transactions on robotics*, vol. 24, no. 1, pp. 65–74, 2008.
- [20] A. Saunders, D. I. Goldman, R. J. Full, and M. Buehler, “The rise climbing robot: body and leg design,” in *Unmanned Systems Technology VIII*, vol. 6230. SPIE, 2006, pp. 401–413.
- [21] M. P. Austin, J. M. Brown, C. A. Young, and J. E. Clark, “Leg design to enable dynamic running and climbing on bobcat,” in *2018 IEEE/RSJ International Conference on Intelligent Robots and Systems*. IEEE, 2018, pp. 3799–3806.

- [22] A. Parness, N. Abcouwer, C. Fuller, N. Wiltsie, J. Nash, and B. Kennedy, "Lemur 3: A limbed climbing robot for extreme terrain mobility in space," in *2017 IEEE international conference on robotics and automation*. IEEE, 2017, pp. 5467–5473.
- [23] K. Nagaoka, H. Minote, K. Maruya, Y. Shirai, K. Yoshida, T. Hakamada, H. Sawada, and T. Kubota, "Passive spine gripper for free-climbing robot in extreme terrain," *IEEE Robotics and Automation Letters*, vol. 3, no. 3, pp. 1765–1770, 2018.
- [24] Y. Tanaka, Y. Shirai, X. Lin, A. Schperberg, H. Kato, A. Swerdlow, N. Kumagai, and D. Hong, "Scaler: A tough versatile quadruped free-climber robot," in *2022 IEEE/RSJ International Conference on Intelligent Robots and Systems*, 2022, pp. 5632–5639.
- [25] Y. Shirai, X. Lin, A. Schperberg, Y. Tanaka, H. Kato, V. Vichathorn, and D. Hong, "Simultaneous contact-rich grasping and locomotion via distributed optimization enabling free-climbing for multi-limbed robots," in *2022 IEEE/RSJ International Conference on Intelligent Robots and Systems*. IEEE, 2022, pp. 13 563–13 570.
- [26] Y. Tanaka, Y. Shirai, Z. Lacey, X. Lin, J. Liu, and D. Hong, "An underactuated whipleretree mechanism gripper based on multi-objective design optimization with auto-tuned weights," in *2021 IEEE/RSJ International Conference on Intelligent Robots and Systems*, 2021, pp. 6139–6146.
- [27] A. Schperberg, Y. Shirai, X. Lin, Y. Tanaka, and D. Hong, "Adaptive force controller for contact-rich robotic systems using an unscented kalman filter," in *2023 IEEE-RAS 23rd International Conference on Humanoid Robots*, 2023.
- [28] P. Dangel, E. Sihite, and A. Ramezani, "Control of thruster-assisted, bipedal legged locomotion of the harpy robot," *Frontiers in Robotics and AI*, vol. 8, 2021. [Online]. Available: <https://www.frontiersin.org/articles/10.3389/frobt.2021.770514>
- [29] K. Kim, P. Spieler, E.-S. Lupu, A. Ramezani, and S.-J. Chung, "A bipedal walking robot that can fly, slackline, and skateboard," *Science Robotics*, vol. 6, no. 59, p. eabf8136, 2021. [Online]. Available: <https://www.science.org/doi/abs/10.1126/scirobotics.abf8136>
- [30] L. Chin, M. Burns, G. Xie, and D. Rus, "Flipper-style locomotion through strong expanding modular robots," *IEEE Robotics and Automation Letters*, vol. 8, no. 2, pp. 528–535, 2023.
- [31] Z. Chen, B. Tighe, and J. Zhao, "Origami-inspired modules enable a reconfigurable robot with programmable shapes and motions," *IEEE/ASME Transactions on Mechatronics*, vol. 27, no. 4, pp. 2016–2025, 2022.
- [32] J. Hooks, M. S. Ahn, J. Yu, X. Zhang, T. Zhu, H. Chae, and D. Hong, "Alphred: A multi-modal operations quadruped robot for package delivery applications," *IEEE Robotics and Automation Letters*, vol. 5, no. 4, pp. 5409–5416, 2020.
- [33] M. Bjelonic, C. D. Bellicoso, Y. de Viragh, D. Sako, F. D. Tresoldi, F. Jenelten, and M. Hutter, "Keep rollin'—whole-body motion control and planning for wheeled quadrupedal robots," *IEEE Robotics and Automation Letters*, vol. 4, no. 2, pp. 2116–2123, 2019.
- [34] M. Polzin, Q. Guan, and J. Hughes, "Robotic locomotion through active and passive morphological adaptation in extreme outdoor environments," *Science Robotics*, vol. 10, no. 99, p. eadp6419, 2025. [Online]. Available: <https://www.science.org/doi/abs/10.1126/scirobotics.adp6419>
- [35] X. Ai, H. Yue, and W. D. Wang, "Crawling soft robot exploiting wheel-legs and multimodal locomotion for high terrestrial maneuverability," *IEEE Transactions on Robotics*, vol. 39, no. 6, pp. 4230–4239, 2023.
- [36] Korea Atomic Energy Research Institute, "Korea atomic energy research institute (kaeri) — english website," <https://www.kaeri.re.kr/eng/>, 2025, accessed: 31 Oct. 2025.
- [37] C. Yu and A. Rosendo, "Multi-modal legged locomotion framework with automated residual reinforcement learning," *IEEE Robotics and Automation Letters*, vol. 7, no. 4, pp. 10 312–10 319, 2022.
- [38] Bota Systems, "Force-torque sensors," <https://www.botasys.com/>, 2025, accessed: July 21, 2025.
- [39] P. Kumar, H. Hirani, and A. Agrawal, "Fatigue failure prediction in spur gear pair using agma approach," *Materials Today: Proceedings*, vol. 4, no. 2, pp. 2470–2477, 2017.
- [40] G. M. Maitra, "Handbook of gear design," 1994.
- [41] W. Močko, "The influence of stress-controlled tensile fatigue loading on the stress-strain characteristics of aisi 1045 steel," *Materials & Design*, vol. 58, pp. 145–153, 2014.
- [42] M. H. Raibert, *Legged Robots That Balance*. USA: Massachusetts Institute of Technology, 1986.
- [43] Y. Zhao, H.-C. Lin, and M. Tomizuka, "Efficient Trajectory Optimization for Robot Motion Planning," in *2018 15th International Conference on Control, Automation, Robotics and Vision (ICARCV)*, 2018, pp. 260–265.
- [44] J. Norby and A. M. Johnson, "Fast global motion planning for dynamic legged robots," in *2020 IEEE/RSJ International Conference on Intelligent Robots and Systems (IROS)*, 2020, pp. 3829–3836.
- [45] S. Kajita, F. Kanehiro, K. Kaneko, K. Fujiwara, K. Harada, K. Yokoi, and H. Hirukawa, "Biped walking pattern generation by using preview control of zero-moment point," in *2003 IEEE International Conference on Robotics and Automation*, vol. 2, 2003, pp. 1620–1626.
- [46] S. Kuindersma, F. Permenter, and R. Tedrake, "An efficiently solvable quadratic program for stabilizing dynamic locomotion," in *2014 IEEE International Conference on Robotics and Automation (ICRA)*, 2014, pp. 2589–2594.
- [47] V. Tsounis, M. Alge, J. Lee, F. Farshidian, and M. Hutter, "Deepgait: Planning and control of quadrupedal gaits using deep reinforcement learning," *IEEE Robotics and Automation Letters*, vol. 5, no. 2, pp. 3699–3706, 2020.
- [48] J. Lee, J. Hwangbo, L. Wellhausen, V. Koltun, and M. Hutter, "Learning quadrupedal locomotion over challenging terrain," *Science Robotics*, vol. 5, no. 47, p. eabc5986, 2020. [Online]. Available: <https://www.science.org/doi/abs/10.1126/scirobotics.abc5986>
- [49] K. Ito and F. Matsuno, "A study of reinforcement learning for the robot with many degrees of freedom - acquisition of locomotion patterns for multi-legged robot," in *Proceedings 2002 IEEE International Conference on Robotics and Automation (Cat. No.02CH37292)*, vol. 4, 2002, pp. 3392–3397 vol.4.
- [50] Z. Liang, S. Zhu, and X. Jin, "Walking parameters design of biped robots based on reinforcement learning," in *Proceedings of the 30th Chinese Control Conference*, 2011, pp. 4017–4022.
- [51] H. Kimura, T. Yamashita, and S. Kobayashi, "Reinforcement learning of walking behavior for a four-legged robot," in *Proceedings of the 40th IEEE Conference on Decision and Control (Cat. No.01CH37228)*, vol. 1, 2001, pp. 411–416 vol.1.
- [52] A. Schperberg, S. Tsuei, S. Soatto, and D. Hong, "Saber: Data-driven motion planner for autonomously navigating heterogeneous robots," *IEEE Robotics and Automation Letters*, vol. 6, no. 4, pp. 8086–8093, 2021.
- [53] E. Vollenweider, M. Bjelonic, V. Klemm, N. Rudin, J. Lee, and M. Hutter, "Advanced skills through multiple adversarial motion priors in reinforcement learning," in *2023 IEEE International Conference on Robotics and Automation (ICRA)*, 2023, pp. 5120–5126.
- [54] A. Escontrela, X. B. Peng, W. Yu, T. Zhang, A. Iscen, K. Goldberg, and P. Abbeel, "Adversarial motion priors make good substitutes for complex reward functions," 2022. [Online]. Available: <https://arxiv.org/abs/2203.15103>
- [55] T. Haarnoja, B. Moran, G. Lever, S. H. Huang, D. Tirumala, J. Humplik, M. Wulfmeier, S. Tunyasuvunakool, N. Y. Siegel, R. Hafner, M. Bloesch, K. Hartikainen, A. Byravan, L. Hasenclever, Y. Tassa, F. Sadeghi, N. Batchelor, F. Casarini, S. Saliceti, C. Game, N. Sreendran, K. Patel, M. Gwira, A. Huber, N. Hurley, F. Nori, R. Hadsell, and N. Heess, "Learning agile soccer skills for a bipedal robot with deep reinforcement learning," *Science Robotics*, vol. 9, no. 89, p. eadi8022, 2024. [Online]. Available: <https://www.science.org/doi/abs/10.1126/scirobotics.adi8022>
- [56] A. Schperberg, Y. Tanaka, F. Xu, M. Menner, and D. Hong, "Real-to-sim: Predicting residual errors of robotic systems with sparse data using a learning-based unscented kalman filter," in *2023 20th International Conference on Ubiquitous Robots*, 2023, pp. 27–34.
- [57] X. Chen, J. Hu, C. Jin, L. Li, and L. Wang, "Understanding domain randomization for sim-to-real transfer," 2022. [Online]. Available: <https://arxiv.org/abs/2110.03239>
- [58] S. Park, J. Kim, and H. J. Kim, "Zero-shot transfer learning of a throwing task via domain randomization," in *2020 20th International Conference on Control, Automation and Systems (ICCAS)*, 2020, pp. 1026–1030.
- [59] Y. Jiang, C. Li, W. Dai, J. Zou, and H. Xiong, "Variance reduced domain randomization for reinforcement learning with policy gradient," *IEEE Transactions on Pattern Analysis and Machine Intelligence*, vol. 46, no. 2, pp. 1031–1048, 2024.
- [60] A. Shakerimov, T. Alizadeh, and H. A. Varol, "Efficient sim-to-real transfer in reinforcement learning through domain randomization and domain adaptation," *IEEE Access*, vol. 11, pp. 136 809–136 824, 2023.
- [61] A. Schwartzwald and N. Papanikolopoulos, "Sim-to-real with domain randomization for tumbling robot control," in *2020 IEEE/RSJ International Conference on Intelligent Robots and Systems (IROS)*, 2020, pp. 4411–4417.
- [62] J. Di Carlo, P. M. Wensing, B. Katz, G. Bledd, and S. Kim, "Dynamic locomotion in the mit cheetah 3 through convex model-predictive control," in *2018 IEEE/RSJ international conference on intelligent robots and systems*. IEEE, 2018, pp. 1–9.

- [63] A. Schperberg, S. D. Cairano, and M. Menner, "Auto-tuning of controller and online trajectory planner for legged robots," *IEEE Robotics and Automation Letters*, vol. 7, no. 3, pp. 7802–7809, 2022.
- [64] X. Lin, F. Xu, A. Schperberg, and D. Hong, "Learning near-global-optimal strategies for hybrid non-convex model predictive control of single rigid body locomotion," 2022. [Online]. Available: <https://arxiv.org/abs/2207.07846>
- [65] E. Garone, S. Di Cairano, and I. Kolmanovsky, "Reference and command governors for systems with constraints: A survey on theory and applications," *Automatica*, vol. 75, pp. 306–328, 2017. [Online]. Available: <https://www.sciencedirect.com/science/article/pii/S0005109816303715>
- [66] I. Kolmanovsky, E. Garone, and S. Di Cairano, "Reference and command governors: A tutorial on their theory and automotive applications," in *2014 American Control Conference*, 2014, pp. 226–241.
- [67] G. Piovan and F. Bullo, "On coordinate-free rotation decomposition: Euler angles about arbitrary axes," *IEEE Transactions on Robotics*, vol. 28, no. 3, pp. 728–733, 2012.
- [68] A. Schperberg, Y. Tanaka, S. Mowlavi, F. Xu, B. Balaji, and D. Hong, "Optistate: State estimation of legged robots using gated networks with transformer-based vision and kalman filtering," *arXiv preprint arXiv:2401.16719*, 2024.
- [69] M. Yaseen, "What is yolov8: An in-depth exploration of the internal features of the next-generation object detector," 2024. [Online]. Available: <https://arxiv.org/abs/2408.15857>
- [70] T. Schouwenaars, B. De Moor, E. Feron, and J. How, "Mixed integer programming for multi-vehicle path planning," in *2001 European Control Conference (ECC)*, 2001, pp. 2603–2608.
- [71] E. Todorov, T. Erez, and Y. Tassa, "Mujoco: A physics engine for model-based control," in *2012 IEEE/RSJ International Conference on Intelligent Robots and Systems*. IEEE, 2012, pp. 5026–5033.
- [72] Gurobi Optimization, LLC, "Gurobi Optimizer Reference Manual," 2024. [Online]. Available: <https://www.gurobi.com>